FISEVIER

Contents lists available at ScienceDirect

International Journal of Machine Tools and Manufacture

journal homepage: http://www.elsevier.com/locate/ijmactool





Intra-wave modulations in milling processes

Guowei Tu^a, Xingjian Dong^{a,*}, Chao Qian^a, Shiqian Chen^b, Lan Hu^c, Zhike Peng^a

- a State Key Laboratory of Mechanical System and Vibration, School of Mechanical Engineering, Shanghai Jiao Tong University, Shanghai, 200240, China
- ^b State Key Laboratory of Traction Power, Southwest Jiaotong University, Chengdu, 610031, China
- ^c Shanghai Aerospace Equipments Manufacturer Co. Ltd., Shanghai, 200245, China

ARTICLE INFO

Keywords:
Milling dynamics
Milling stability
Chatter
Intra-wave modulations
Nonlinear chirp mode decomposition

ABSTRACT

Intra-wave modulation effects with oscillating time-varying frequencies have been observed in physical systems including mechanical, ocean, power, and even biological ones. Such phenomena correspond to actual physical processes with which the underlying dynamics of these systems can be understood. In this work, we study intra-wave modulation effects in milling processes with the aid of iterative nonlinear chirp mode decomposition (INCMD), a recently proposed technique for analyzing complex dynamic responses. A nonlinear non-stationary template signal is provided to model milling vibration responses, and an INCMD-based strategy is developed to extract embedded modulation features. Through dynamic simulations and experimental verification, it has been demonstrated that distinct intra-wave modulation frequencies that are exactly equal to theoretical chatter frequencies calculated based on the Floquet theory exist to indicate different cutting states, and milling instability is accompanied by the variation of such a characteristic quantity. Bessel functions can mathematically relate explicit modulation patterns with intricate spectral distributions of milling responses. Moreover, the switch of the modulation pattern, which remains noticeable in the presence of noise, emerges far earlier than visible chatter marks do, indicating the superiority of the chatter detection and even prediction utilizing intra-wave modulation features.

1. Introduction

Milling, especially high-speed milling, is an important precision machining technology [1]. Understanding milling dynamics has always been vital because it is the basis for related industrial applications such as system monitoring [2], prediction [3], and control [4]. Numerous factors, including the parametric excitation due to periodic cutting in and out of tool teeth, time-delay caused by regenerative effects [5], and nonlinearity originating from deformations of processed materials [6], make the milling system a complex one. Such complexity will be exacerbated by chatter, a notorious instability phenomenon in milling processes, especially when the workpiece is a thin-walled part with low stiffness [7].

Forward and reverse system characterization methods can be used to gain insights into milling dynamics. One of the most mature forward techniques is lobe diagram plotting [8], which predicts system stability from the perspective of dynamical bifurcations. Although many strategies exist, a generic approach to obtain the lobe diagram is

semi-discretization [9], which is based on the Floquet theory of periodic time-varying ordinary differential equations. Stability lobes, although helpful in theoretical studies, are difficult to put into practice because of their vulnerability to volatile system parameters and demand for highly accurate system identifications [1]. Other forward schemes based on the mathematical model of physical systems have similar drawbacks.

Reverse characterization aims to comprehend underlying processes through external system responses, among which vibration-related responses, including milling forces [10], displacements [11], accelerations [12], and noises [13], are most commonly utilized because they are easy to collect and are rich in cutting state information. Vibrations emanating from complex milling systems are quite intricate and require the use of signal processing tools. Based on the classic Fourier analysis, the power spectra of milling responses have been employed to explore the essence of perplexing phenomena, including the bifurcation of milling responses [14], influence of tool runout on chatter instability [15], emergence of modal coupling [16], and mechanism of process damping [17].

Nonetheless, the pure frequency-domain description is not an

^{*} Corresponding author. State Key Laboratory of Mechanical System and Vibration, School of Mechanical Engineering, Shanghai Jiao Tong University (Minhang Campus), No. 800, Dongchuan Road, Shanghai, 200240, China.

E-mail addresses: guoweitu@sjtu.edu.cn (G. Tu), donxij@sjtu.edu.cn (X. Dong), qianchao@sjtu.edu.cn (C. Qian), chenshiqian@swjtu.edu.cn (S. Chen), 13512105097@126.com (L. Hu), z.peng@sjtu.edu.cn (Z. Peng).

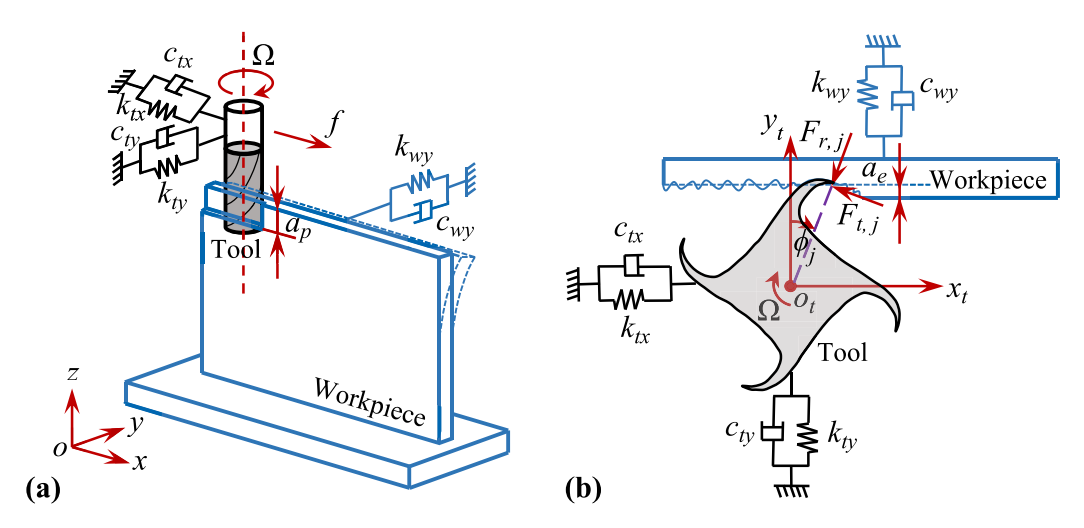


Fig. 1. Schematic of the thin-walled part milling system [32]. (a) Overall view. (b) Top view.

appropriate choice considering the strongly non-stationary attributes of the milling system, which limits the application of traditional spectrum tools. According to the Floquet theory [14], infinite harmonics associated with stable milling exist in the frequency domain. Even more inexplicable components arise when chatter occurs, making the spectral distribution complicated. Such characterizations are mathematically rigorous though, they do not correspond to actual physical processes; that is, they are extrinsic features and do not reflect the nature of the milling system. As a result, subtle changes in the cutting state will be barely captured by the power spectrum because extrinsic features lag intrinsic processes. A new cutting state cannot be detected until it is fully developed, especially in practical engineering problems with interferences and noises [18].

As an alternative to the frequency-domain analyses, time-domain periodic sampling approaches such as the Poincaré mapping [19] have been utilized to capture phase-space milling bifurcations. Such techniques have extremely low computational costs and thus can be employed for rapid dynamic analyses with the aid of a dedicated numeric metric [20]. However, when the cutting is in the critical transition phase, the evolution of sampling points in the phase space cannot be traced effectively and the corresponding metric threshold is difficult to determine. In other words, chatter is difficult to detect in the premature phase.

A class of novel dynamic characterizations named intra-wave modulations were first utilized by Huang et al. (1996) [21] to analyze responses from classical Duffing, Rössler, and Lorenz systems, and the method has recently gained much attention. Neither providing spurious nor redundant information, intra-wave modulation analyses conduce to the intuitive understanding of physical systems. Such features are directly associated with underlying dynamic processes such as rubbing impacts in rotor systems [22], crack-induced large deformations in beam systems [23], inter-area oscillations in power systems [24], rogue waves in ocean systems [25], and even repetitive movements in human biological systems [26]. However, intra-wave modulated signals exhibit a fast oscillating time-varying frequency in the time-frequency domain [23]. Additionally, in complex systems, responses from different origins tend to be coupled. Considering these two factors, an effective tool that integrates the functions of signal decomposition and time-frequency analysis is needed. Although the classic Hilbert-Huang transform (HHT) [21] meets the above needs, it lacks a rigorous mathematical foundation and thus is extremely sensitive to perturbations of noise. Narrow-band filter-bank-based variational mode decomposition (VMD) [27] and synchrosqueezing transform (SST) [28] cannot work in such cases because intra-wave modulation effects lead to wide-band spectra [22].

Conventional simple descriptive models of milling responses can

only characterize milling processes of a particular aspect and thus impede a comprehensive understanding of milling dynamics. Combining the time, frequency, and amplitude domain, the characterization of milling processes based on intra-wave modulations can be expected to provide new insights but has never been studied. Related to intra-wave modulation phenomena, some questions are to be tackled:

- What is the physics of intra-wave modulations in milling processes?
- Do distinct modulation patterns exist under different cutting states?
- Is there any internal relationship between the modulation patterns, spectral distributions, and dynamical bifurcations?
- What can we utilize intra-wave modulations of milling responses for?

In this work, to answer these questions, a generalized nonlinear non-stationary signal model of milling responses is established first. Determination of model parameters is equivalent to the extraction of embedded intra-wave modulation features, to accomplish which, a lack of an effective signal processing tool has to be addressed. A novel strategy based on the recently proposed iterative nonlinear chirp mode decomposition (INCMD) [23] is developed. The idea of the INCMD is a blend of those adopted in the VMD and HHT. Such a framework makes the INCMD retain both mathematical rigor and algorithm adaptability. An example of a Stokes wave [29] is presented to demonstrate that the INCMD achieves a physically meaningful decomposition for wide-band multicomponent responses [23].

Through dynamic simulations and experimental verification, it has been observed that infinite harmonic processes do not exist in stable cutting, but are induced by intra-wave modulated responses with the tooth-passing frequency as the modulation frequency, and such phenomena physically correspond to the stiffening effect [30] caused by cutting impacts. The onset of chatter is intrinsically accompanied not by the emergence of spurious non-harmonic processes, but by the switch of the modulation frequency, and this frequency is exactly equal to the chatter frequency derived from bifurcation calculations based on the Floquet theory [14]. Distinct modulation patterns and spectral distributions can be mathematically related by Bessel functions [31]. Moreover, the switch of the modulation pattern foretells the transition of the cutting state, which emerges far earlier than visible chatter marks do. The findings from this study provide additional insights into the relationship between milling responses and cutting stability, and further demonstrate the application of intra-wave modulation analyses in condition monitoring of milling processes.

2. Dynamics of milling

Chatter is extremely common in the milling of thin-walled parts [1].

A descriptive model of such processes is provided in this section, followed by a simplified stability analysis.

2.1. Dynamic model

A schematic of the milling system is shown in Fig. 1. The tool is modeled as a two-degree-of-freedom spring-mass-damper system, and the thin-walled workpiece is represented by a cantilevered plate with a single main mode of vibration [32]. The motion of the workpiece is considered in an inertial coordinate system with the point o as the origin (see Fig. 1 (a)), while that of the tool is considered in a non-inertial coordinate system attached to its own geometric center o_t (see Fig. 1 (b)). The spindle rotation and feed motion indicate an up-milling operation. The engagement between the tool and the workpiece is governed by

$$\begin{cases} m_{tx}\ddot{x}_{t} + c_{tx}\dot{x}_{t} + k_{tx}x_{t} = F_{x}(t), \\ m_{ty}\ddot{y}_{t} + c_{ty}\dot{y}_{t} + k_{ty}y_{t} = F_{y}(t), \\ m_{wy}\ddot{y}_{w} + c_{wy}\dot{y}_{w} + k_{wy}y_{w} = -F_{y}(t), \end{cases}$$
(1)

where y_t , x_t , m_{ty} , m_{tx} , k_{ty} , k_{tx} , c_{ty} , and c_{tx} denote the displacement, mass, stiffness, and damping coefficient of the tool in the feed and its normal direction, respectively, while y_w , m_{wy} , k_{wy} , and c_{wy} are those of the workpiece in the normal direction. Moreover, $F_x(t)$ and $F_y(t)$ are the cutting forces in two orthogonal directions, which must be determined to explicitly express Eq. (1).

Considering an N-teeth milling tool, for the j-th tooth engaged as shown in Fig. 1 (b), the cutting force can be projected in the radial and tangential directions as

$$\begin{cases} F_{t,j}(t) = \kappa_t a_p h_j(t), \\ F_{r,j}(t) = \kappa_n \kappa_t a_p h_j(t), \end{cases}$$
 (2)

where κ_t is the specific cutting energy, κ_n is a proportionality factor, a_p is the axial depth of cut (see Fig. 1 (a)), and $h_j(t)$ denotes the chip thickness encountered by tooth j at time t. Consisting of a static part corresponding to the tool feed and a dynamic part resulting from the *regenerative effect* [33], the term $h_i(t)$ is expressed by

$$\begin{cases} h_j(t) = h_{j,stat}(t) + h_{j,dyn}(t) = f_z \sin(\varphi_j(t)) + (\Delta x(t) \sin(\varphi_j(t)) + \Delta y(t) \cos(\varphi_j(t))), \\ \Delta x(t) = x_t(t) - x_t(t-\tau), \Delta y(t) = (y_t(t) - y_w(t)) - (y_t(t-\tau) - y_w(t-\tau)), \end{cases}$$
(3)

where f_z is the feed per tooth, τ is the tooth passing period such that $\tau=60/N\Omega$ in which Ω denotes the spindle speed in rpm, and $\varphi_j(t)$ represents the angular position of the tooth j at time t as $\varphi_j(t)=(2\pi\Omega t/60)-2\pi(j-1)/N, j=1,2,\cdots,N$. Applying the projection transformation, the cutting force in the feed direction and its normal direction can be obtained as

$$\begin{cases}
F_{x,j}(t) = -F_{r,j}(t)\sin(\varphi_j(t)) - F_{t,j}(t)\cos(\varphi_j(t)), \\
F_{y,j}(t) = -F_{r,j}(t)\cos(\varphi_j(t)) + F_{t,j}(t)\sin(\varphi_j(t)).
\end{cases}$$
(4)

The cutting force acting on the entire tool can be determined as

$$\begin{cases} F_{x}(t) = \sum_{j=1}^{N} g(\varphi_{j}(t))\delta(h_{j}(t))F_{x,j}(t), \\ F_{y}(t) = \sum_{j=1}^{N} g(\varphi_{j}(t))\delta(h_{j}(t))F_{y,j}(t). \end{cases}$$
(5)

The function $g(\cdot)$ in Eq. (5) is a tooth-cutting indicating function given by

$$g(\varphi_j(t)) = \begin{cases} 1, & \varphi_{st} < \varphi_j(t) < \varphi_{ex} \\ 0, & \text{else} \end{cases}, \tag{6}$$

where φ_{st} and φ_{ex} are the cutting start and exit angle, respectively, given

Table 1Simulation parameters of the milling system [6].

	Mass (kg)	Stiffness (N m^{-1})	Damping (N s m^{-1})
Tool (x)	2.01×10^{-2}	4.14×10^5	1.56
Tool (y)	1.99×10^{-2}	4.09×10^5	1.60
Workpiece (y)	56.75	7.15×10^6	1.68×10^3

by $\varphi_{st}=0$ and $\varphi_{ex}=\cos(1-2a_e/D)$ in a standard up-milling process. Here, a_e is the radial depth of cut (see Fig. 1 (b)) and D is the tool diameter. In addition, $\delta(\cdot)$ is another indicating function that characterizes the loss-of-contact effect [34] between the tool and the workpiece, which can dominate the system dynamics in a partial immersion milling process. The function $\delta(\cdot)$ is expressed as [34].

$$\delta(h_j(t)) = \begin{cases} 1, & h_j(t) > 0 \\ 0, & h_j(t) \le 0 \end{cases}$$
 (7)

Substituting Eqs. (2)–(7) into Eq. (1), the explicit governing equation can be formulated, leading to a piecewise-linear, periodically time-varying, constant-time-delay six-dimensional state-space system.

2.2. Stability and spectral distributions

Disregarding the nonlinearity in Eq. (1), the well-known semi-discretization method [9] is applied to achieve a simplified stability analysis. A milling process of a thin-walled aluminum plate that was already studied numerically by Balachandran [6] is considered. The tool is assumed to have only one tooth to exclude the *run-out effect* [15], and the tool diameter is taken as 8 mm. The specific cutting energy $\kappa_t = 644$ MPa and proportionality factor $\kappa_n = 0.37$. The immersion ratio (i.e. a_e/D) is considered to be 0.05, and the feed rate is held constant at 0.01 mm/tooth. Other simulation parameters are listed in Table 1, and a high-speed milling process with $\Omega = 1 \times 10^4 \sim 2.6 \times 10^4$ rpm is analyzed.

Fig. 2 demonstrates the stability of the milling system. Using the semi-discretization, the instability type and the corresponding chatter frequencies, in addition to the stability itself, can be determined by analyzing the eigenvalues of the Floquet transition matrix [14]. As demonstrated in Fig. 2 (a), the stable and chatter regions are bounded by the solid black line. Red and green dots denote the Neimark-Sacker bifurcation lobes that lead to the quasi-periodic chatter and flip bifurcation lobes that lead to the periodic-2 chatter, where the eigenvalues penetrate the unit circle in the negative real and conjugate complex forms, respectively [35]. Lens-like structures with periodic-2 and quasi-periodic boundaries as the bottom and upper arcs illustrate a transition from premature to fully developed chatter, which is a common scenario in low-immersion milling [35]. In this regard, periodic-2 motion acts as a presage of the final malfunction. Four different cutting conditions with corresponding eigenvalues, denoted as A $(\Omega = 1 \times 10^3 \text{ rpm}, a_p = 1 \text{ mm}), \text{ B } (\Omega = 13 \times 10^3 \text{ rpm}, a_p = 1.7 \text{ mm}), \text{ C}$ ($\Omega = 17 \times 10^3$ rpm, $a_p = 2.5$ mm), and D ($\Omega = 25 \times 10^3$ rpm, $a_p = 1.05$ mm) in Fig. 2 (a), respectively, indicate the typical stable, pre-instability, chatter, and post-instability states.

In this study, particular attention is given to the distinct spectral structures of the responses under different states. Denoting the chatter frequency¹ with f_c , the spectral components arising in the stable, quasiperiodic, and periodic-2 responses, respectively, are given by (where "TP" stands for "tooth passing") [14]

¹ Note that the chatter frequency herein follows the definition in the numerical semi-discretization analysis [14]. It is not necessarily the peak frequency in the spectrum when chatter occurs as specified in many papers where the analytical stability analysis is used [48].

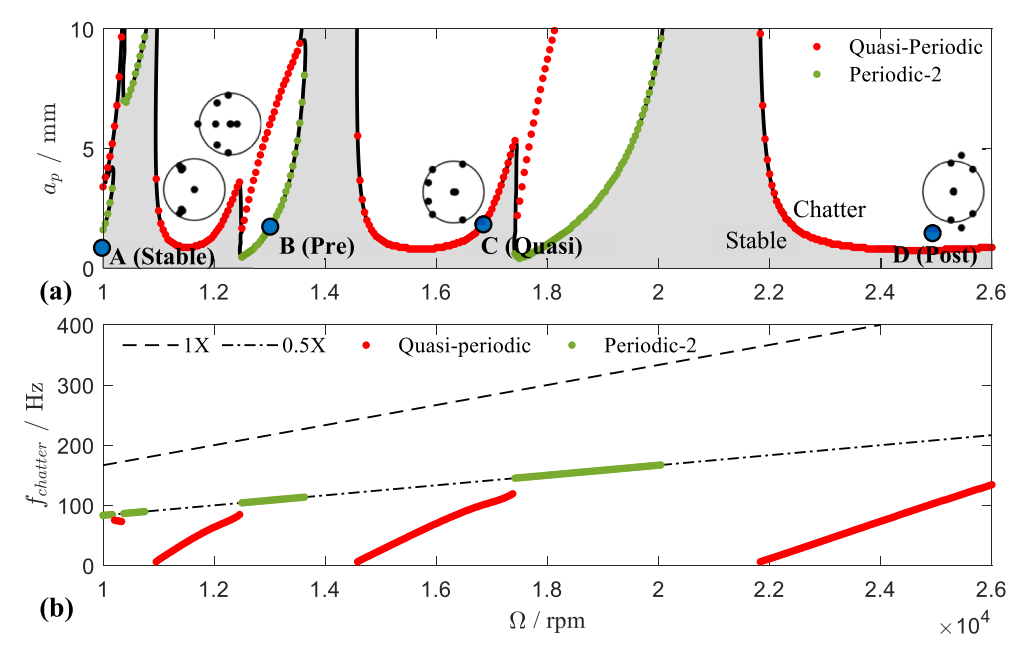


Fig. 2. Stability of the milling system. (a) Stability lobe. (b) Chatter frequencies (1X and 0.5X stand for the tooth passing frequency and half of the tooth passing frequency respectively).

$$f_{stable} = \{kf_{TP}\} = \left\{\frac{kN\Omega}{60}\right\} \text{ (Hz)}, \quad k = 0, \pm 1, \pm 2, \cdots,$$

$$f_{quasi} = \left\{\frac{kN\Omega}{60} \pm f_{c,quasi}\right\} \text{ (Hz)}, \quad k = 0, \pm 1, \pm 2, \cdots,$$

$$f_{p-2} = \left\{\frac{kN\Omega}{60} \pm f_{c,p-2}\right\} = \left\{\frac{kN\Omega}{60} \pm \frac{N\Omega}{120}\right\} \text{ (Hz)}, \quad k = 0, \pm 1, \pm 2, \cdots,$$
(8)

where the chatter frequency of the quasi-periodic type is an irrational multiple (i.e., λf_{TP} where λ denotes an irrational number between 0 and 1), while that of the periodic-2 type is exactly half of the tooth-passing frequency (i.e., $0.5f_{TP}$), as shown in Fig. 2 (b).

As Eq. (8) demonstrates, infinite harmonics exist in the spectrum during stable cutting, and more complex components appear when chatter occurs, leading to an intricate spectral distribution. Such features are not physically meaningful [21]. An intrinsic interpretation of milling responses can be achieved by applying the signal model of intra-wave modulations, a class of inherent characteristics in dynamical systems [21]. Such a model, along with an efficient approach to extract the embedded intra-wave modulation features, will be introduced in Section 3.

3. Methodology

3.1. Signal model

The response signal from the milling system has strongly timevarying attributes, and can be modeled as [23].

$$s(t) = \sum_{k=1}^{K} c_k(t) = \sum_{k=1}^{K} a_k(t) \cos\left(2\pi \int_0^t f_k(\tau) d\tau + \phi_k\right), \tag{9}$$

where a total of K so-called *nonlinear chirp modes* [36] constitute the signal. The initial phase, instantaneous amplitude (IA), and instantaneous frequency (IF) of the k-th mode $c_k(t)$ are denoted by ϕ_k , $a_k(t)$, and $f_k(t)$, respectively. In terms of intra-wave modulations, model Eqn (9) can be further specified as [23]

$$s(t) = \sum_{k=1}^{K} w_k(t) = \sum_{k=1}^{K} a_k(t) \cos\left(2\pi f_{base,k} t + \varepsilon_{FM,k} \sin\left(2\pi f_{FM,k} t + \theta_k\right) + \phi_k\right),$$
(10)

where the IF of the k-th intra-wave modulated mode $w_k(t)$, a particular family of nonlinear chirp modes [36], is given by

$$f_k(t) = f_{base,k} + \varepsilon_{FM,k} f_{FM,k} \cos(2\pi f_{FM,k} t + \theta_k), \tag{11}$$

which demonstrates an IF oscillating sinusoidally around the center value $f_{base,k}$, with $f_{FM,k}$ as the frequency, $\varepsilon_{FM,k}f_{FM,k}$ as the range, and θ_k as the initial phase. Using Bessel functions [31], a series expansion of the mode $w_k(t)$ can be expressed as

$$w_k(t) = \sum_{i=1}^{+\infty} J_n(\varepsilon_{FM,k}) \{ a_k(t) \cos(2\pi (f_{base,k} + nf_{FM,k}) t + n\theta_k + \phi_k) \}, \tag{12}$$

where $J_n(\cdot)$ represents the Bessel function of the first kind and the n-th order [31].

Infinitely many sidebands centered on $f_{base,k}$ (see Eq. (12)) justify the mathematical consistency between the intra-wave modulated mode and the spectral distribution discussed in Section 2.2. Further investigation is necessary to determine a deeper relationship that links the modulation patterns with cutting states. However, analysis of such signals is a tricky problem. Multiple wide-band modes $w_k(t)$, $k=1,2,\cdots,K$ in the signal Eqn (10) cumulatively lead to an overlapped spectrum. Therefore, narrow-band filter-bank-based methods such as VMD [27] cannot work in such circumstances. The well-known HHT [21] technique, proficient in addressing such situations though, is difficult to put into practice because of its extremely low robustness. The recently proposed INCMD approach [23] that combines the ideas of VMD and HHT is particularly designed to analyze wide-band multicomponent signals. Based on INCMD, the development of an effective strategy for capturing intra-wave modulations is described in Sub-section 3.2.

3.2. Iterative nonlinear chirp mode decomposition (INCMD)-based strategy for capturing intra-wave modulations

Similar to the VMD [27], the INCMD [23] addresses the problem of signal mode reconstruction under the framework of variational optimization. Both following the idea of *demodulating each mode and minimizing its bandwidth* [27], distinctions between these two methods lie in the demodulation strategy itself. Unlike the pure frequency-shift operation implemented in the VMD, the INCMD manages to find a frequency

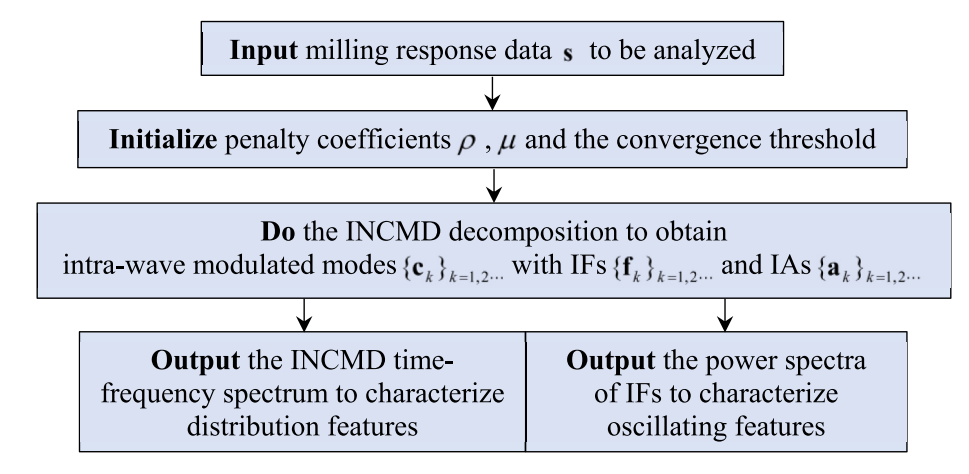


Fig. 3. Flow chart of the proposed INCMD-based strategy for capturing intra-wave modulations.

function $\widetilde{f}_k(t)$ such that a pair of fully demodulated modes based on the signal model Eqn (9) can be obtained as [23]

$$c_k^{d_1}(t) = a_k(t)\cos\left(2\pi \int_0^t \left(f_k(\tau) - \widetilde{f}_k(\tau)\right) d\tau + \phi_k\right),$$

$$c_k^{d_2}(t) = -a_k(t)\sin\left(2\pi \int_0^t \left(f_k(\tau) - \widetilde{f}_k(\tau)\right) d\tau + \phi_k\right).$$
(13)

Through the re-modulation of the quadrature constituents $c_k^{d_1}(t)$ and $c_k^{d_2}(t)$ in Eq. (13), the reconstructed mode $c_k(t)$ can be expressed as

$$c_k(t) = c_k^{d_1}(t)\cos\left(2\pi\int_0^t \widetilde{f}_k(\tau)d\tau\right) + c_k^{d_2}(t)\sin\left(2\pi\int_0^t \widetilde{f}_k(\tau)d\tau\right),\tag{14}$$

based on which the IA function $a_k(t)$ is given by

$$a_k(t) = \sqrt{\left(c_k^{d_1}(t)\right)^2 + \left(c_k^{d_2}(t)\right)^2}.$$
 (15)

Ideal demodulation can be achieved when the estimated IF $\widetilde{f}_k(t)$ is exactly the true IF $f_k(t)$ itself, where $c_k^{d_1}(t)$ and $c_k^{d_2}(t)$ will have the most compact spectrum [36]. In this regard, the optimal $f_k(t)$ can be determined by solving an optimization problem as [23]

$$\min_{\substack{c_k^{d_1}(t), c_k^{d_2}(t), \widetilde{f}_k(t)}} \left\{ \left\| c_k^{d_1''}(t) \right\|_2^2 + \left\| c_k^{d_2''}(t) \right\|_2^2 \right\}, \\
\text{s.t. } s_c(t) = c_k^{d_1}(t) \cos\left(2\pi \int_0^t \widetilde{f}_k(\tau) d\tau\right) + c_k^{d_2}(t) \sin\left(2\pi \int_0^t \widetilde{f}_k(\tau) d\tau\right) + c_{res},$$
(16)

where the squared ℓ_2 norm of the second-order derivative (i.e., $\|(\cdot)''\|_2^2$) acts as an operator to evaluate the mode bandwidth [23], and c_{res} is the residual after the mode $c_k(t)$ is removed from the current signal $s_c(t)$. To extract modes in the descending order of energy, a greedy optimizer is applied where the objective function to be minimized can be expressed as [23]

$$W_{\rho}\left(\mathbf{c}_{k}^{\mathbf{d}_{1}},\ \mathbf{c}_{k}^{\mathbf{d}_{2}},\ \widetilde{\mathbf{f}}_{k}\right) = \left\|\mathbf{D}\mathbf{c}_{k}^{\mathbf{d}_{1}}\right\|_{2}^{2} + \left\|\mathbf{D}\mathbf{c}_{k}^{\mathbf{d}_{2}}\right\|_{2}^{2} + \rho\left\|\mathbf{s}_{\mathbf{c}} - \left(\boldsymbol{\varphi}_{k}^{\mathbf{1}}\mathbf{c}_{k}^{\mathbf{d}_{1}} + \boldsymbol{\varphi}_{k}^{2}\mathbf{c}_{k}^{\mathbf{d}_{2}}\right)\right\|_{2}^{2}, \quad (17)$$

which is in the discrete-time form with ρ denoting a penalty coefficient, **D** representing a second-order difference matrix, and ϕ_k^1 , ϕ_k^2 being two phase matrices given by

$$\Phi_k^1 = diag[\cos(\beta_k(t_0)), \cos(\beta_k(t_1)), \dots, \cos(\beta_k(t_{N-1}))],
\Phi_k^2 = diag[\sin(\beta_k(t_0)), \sin(\beta_k(t_1)), \dots, \sin(\beta_k(t_{N-1}))],$$
(18)

where $\beta_k(t) = 2\pi \int_0^t \widetilde{f}_k(\tau) d\tau$.

The constrained optimization problem (17) is addressed using the efficient alternating direction method of multipliers (ADMM) [37]. Optimal solutions for $\mathbf{c}_k^{\mathbf{d}_1}$, $\mathbf{c}_k^{\mathbf{d}_2}$ and \mathbf{f}_k can be updated iteratively as [23]

$$\mathbf{c}_{k}^{\mathbf{d}_{1}^{*}} = \mathbf{c}_{k}^{\mathbf{d}_{1}} \Big|_{\partial w_{\rho} \left(\mathbf{c}_{k}^{\mathbf{d}_{1}}, \mathbf{c}_{k}^{\mathbf{d}_{2}}, \widetilde{\mathbf{f}_{k}}\right) / \partial \mathbf{c}_{k}^{\mathbf{d}_{1}} = 0} = \left(\left(\mathbf{\phi}_{k}^{1}\right)^{T} \mathbf{\phi}_{k}^{1} + \frac{1}{\rho} \mathbf{D}^{T} \mathbf{D}\right)^{-1} \left(\mathbf{\phi}_{k}^{1}\right)^{T} \mathbf{s}_{\mathbf{c}},$$

$$\mathbf{c}_{k}^{\mathbf{d}_{2}^{*}} = \mathbf{c}_{k}^{\mathbf{d}_{2}} \Big|_{\partial w_{\rho} \left(\mathbf{c}_{k}^{\mathbf{d}_{1}}, \mathbf{c}_{k}^{\mathbf{d}_{2}}, \widetilde{\mathbf{f}_{k}}\right) / \partial \mathbf{c}_{k}^{\mathbf{d}_{2}} = 0} = \left(\left(\mathbf{\phi}_{k}^{2}\right)^{T} \mathbf{\phi}_{k}^{2} + \frac{1}{\rho} \mathbf{D}^{T} \mathbf{D}\right)^{-1} \left(\mathbf{\phi}_{k}^{2}\right)^{T} \mathbf{s}_{\mathbf{c}},$$

$$\mathbf{f}_{k}^{*} = \mathbf{f}_{k} + \left(\mathbf{I} + \frac{2}{\mu} \mathbf{D}^{T} \mathbf{D}\right)^{-1} \Delta \mathbf{f}_{k}^{*},$$
(19)

with

$$\Delta f_{k}^{*}\left(t\right) = -\tan^{-1}\left(\frac{c_{k}^{d_{2}^{*}}(t)}{c_{k}^{d_{1}^{*}}(t)}\right)' = \frac{1}{2\pi} \frac{c_{k}^{d_{1}^{*'}}(t)c_{k}^{d_{2}^{*}}(t) - c_{k}^{d_{2}^{*'}}(t)c_{k}^{d_{1}^{*}}(t)}{\left(\left(c_{k}^{d_{1}^{*}}(t)\right)^{2} + \left(c_{k}^{d_{2}^{*}}(t)\right)^{2}\right)}, \quad (20)$$

where I represents an identity matrix and μ denotes another penalty coefficient. Detailed derivations of Eqs. (19) and (20) are available in Ref. [23]. By substituting the latest available updates, the k-th mode can be reconstructed as

$$\mathbf{c}_{k}^{*} = \mathbf{\phi}_{k}^{1^{*}} \mathbf{c}_{k}^{\mathbf{d}_{1}^{*}} + \mathbf{\phi}_{k}^{2^{*}} \mathbf{c}_{k}^{\mathbf{d}_{2}^{*}}. \tag{21}$$

To initiate these iterative updates, the peak frequency of the power spectrum of the current signal s_c is obtained as a constant initial IF f_k^0 , and the relative difference between the two latest updated modes is considered as the convergence criterion expressed as

$$\left\|\mathbf{c}_{k}^{i}-\mathbf{c}_{k}^{i-1}\right\|_{2}^{2}\left/\left\|\mathbf{c}_{k}^{i-1}\right\|_{2}^{2}\leqslant\varepsilon.$$
(22)

The termination of the decomposition process is controlled by the result of the Ljung-Box Q-test [23] of the current signal $\mathbf{s_c}$ (i.e., the mode number K is automatically determined [23]). Applying the INCMD technique, all nonlinear modes $\{\mathbf{c}_k\}$ with their IAs $\{\mathbf{a}_k\}$ and IFs $\{\mathbf{f}_k\}$ can be obtained.

Considering intra-wave modulations in signal model Eqn (10), distribution characteristics including $\{a_k\}$, $\{f_{base,k}\}$, and $\{\phi_k\}$ can be analyzed using a two-dimensional INCMD spectrum as

$$Spec(\mathbf{t}_i, \mathbf{f}_j) = \sum_{k=1}^{K} \mathbf{a}_{k,i} \delta(\mathbf{f}_j - \mathbf{f}_{k,j}),$$
(23)

where $i=0,1,\cdots,N_1-1, j=0,1,\cdots,N_2-1$ denotes a $N_1\times N_2$ time-frequency mesh plane and δ is the Dirac delta function. Oscillation

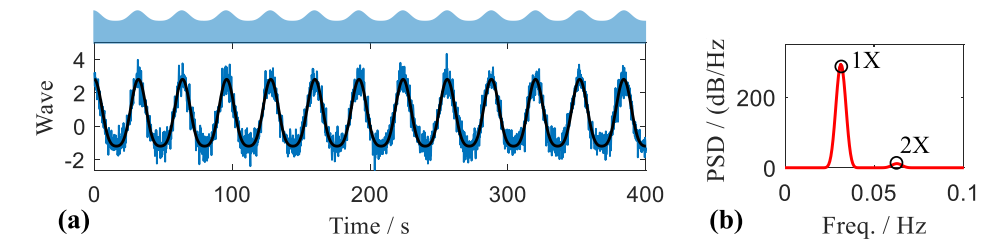


Fig. 4. Stokes wave [29]. (a) Temporal waveform (the blue line denotes noisy version while the black line denotes noise-free version). (b) Power spectrum (noise-free version only). (For interpretation of the references to color in this figure legend, the reader is referred to the Web version of this article.)

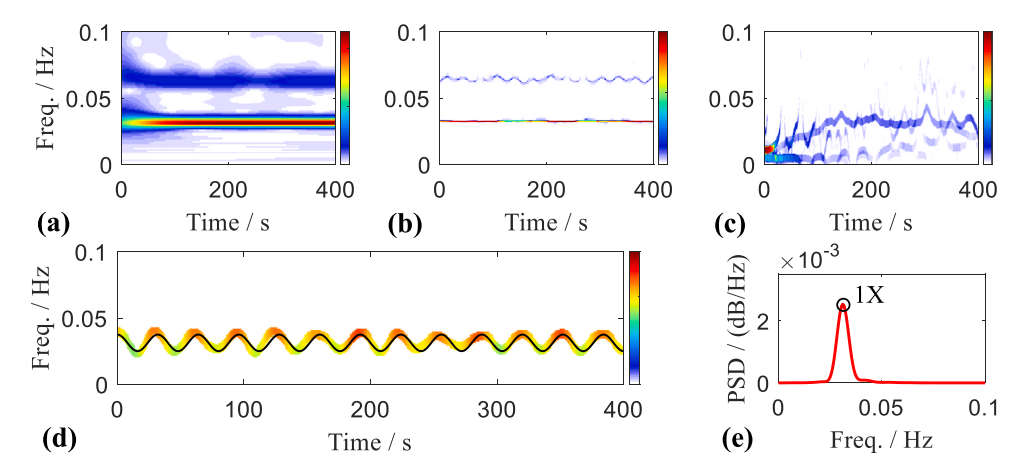


Fig. 5. Time-frequency analysis of the noisy Stokes wave using different tools. (a) Morlet scalogram. (b) SST spectrum. (c) HHT spectrum. (d) INCMD spectrum (the black line denotes the theoretical IF obtained in Eq. (26)). (e) Power spectrum of the IF extracted from the INCMD spectrum.

characteristics including $\{\varepsilon_{FM,k}\}$, $\{f_{FM,k}\}$, and $\{\theta_k\}$ can be analyzed through the Fourier analysis of extracted IFs $\{\mathbf{f}_k\}$ (i.e., power spectra of $\{\mathbf{f}_k\}$), according to Eq. (11). The entire strategy for capturing the intrawave modulations is illustrated in Fig. 3.

3.3. An example: Stokes wave

We provide an example to demonstrate the effectiveness of the above strategy. A classic second-order Stokes wave, which is a perturbation series approximation of nonlinear marine wave motion [29], is

expressed as

$$S(t) = \frac{1}{2}a^{2}k + a\cos\omega t + \frac{1}{2}a^{2}k\cos 2\omega t,$$
 (24)

where a denotes the wave amplitude, ω is the angular frequency, and k is the wavenumber. Taking a=2, $\omega=2\pi/32$ rad s⁻¹, and k=0.2, the temporal waveform is generated as shown in Fig. 4 (a), where the white Gaussian noise with a standard deviation of 0.5 is added to the original signal (black line) to obtain the noisy version (blue line).

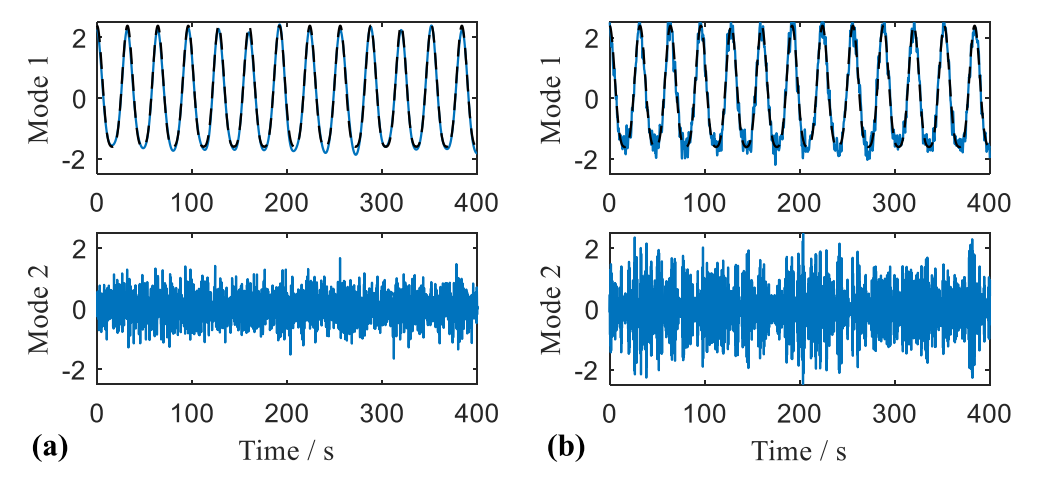


Fig. 6. Signal decompositions of the noisy Stokes wave using different tools. (a) INCMD. (b) VMD. In Mode 1 the solid blue line denotes the extracted mode while the broken black line denotes the noise-free Stokes wave. (For interpretation of the references to color in this figure legend, the reader is referred to the Web version of this article.)

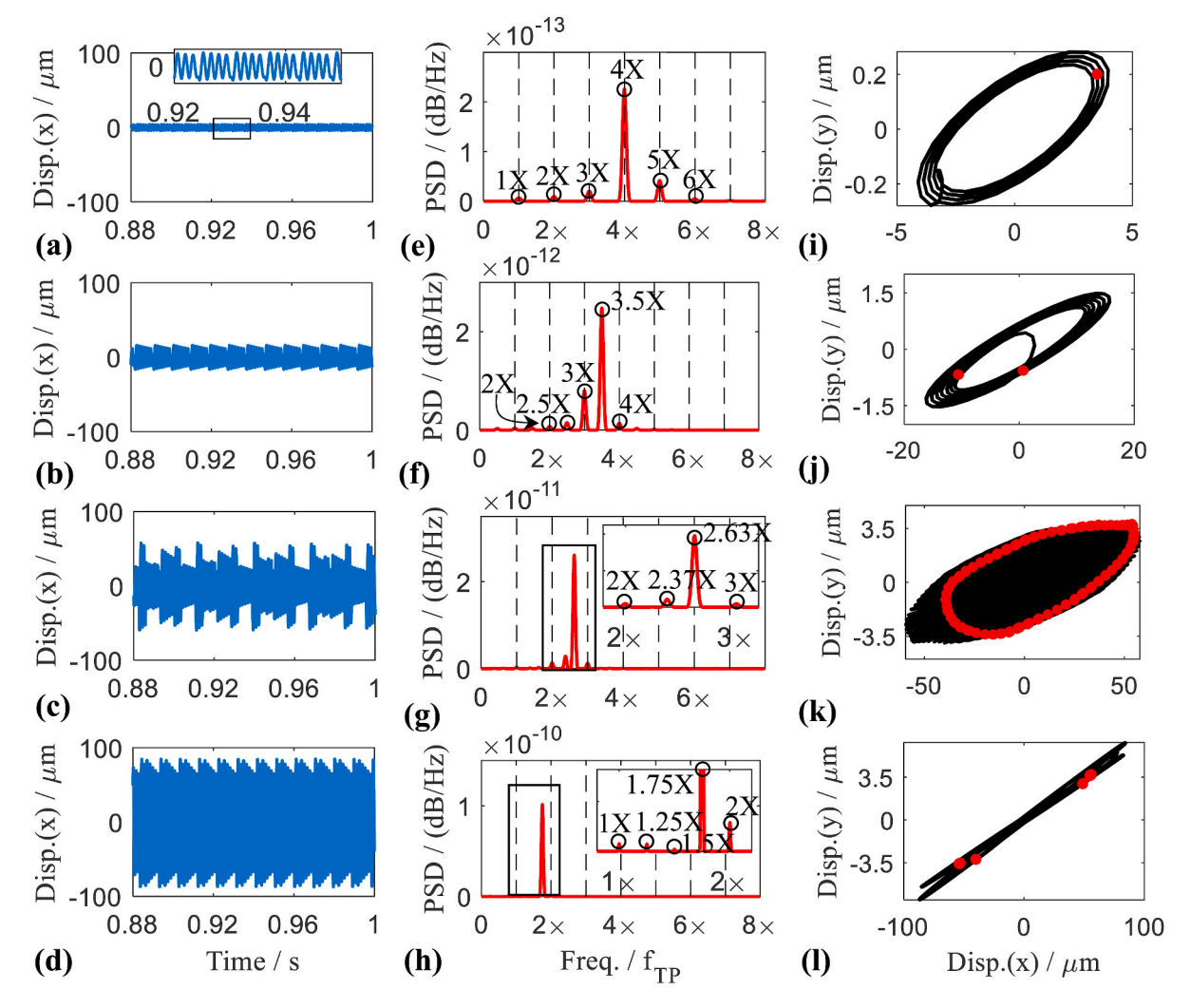


Fig. 7. Studied tool vibrations. (a, b, c, d) Temporal waveforms. (e, f, g, h) Power spectra (dashed black lines denote the tooth-passing frequency and its multiples). (i, j, k, l) Phase portraits (red dots represent the Poincaré mapping). Four sets of responses from the top to the bottom correspond to the stable, pre-instability, chatter, and post-instability state, marked with A, B, C, and D, respectively, in Fig. 2. Simulation duration is taken as 0–1 s and the steady-state during 0.88–1 s is truncated for analyses. (For interpretation of the references to color in this figure legend, the reader is referred to the Web version of this article.)

The power spectrum of the wave signal (see Fig. 4 (b)) presents a superposition of two harmonics, which agrees mathematically with Eq. (24). However, such interpretations make no physical sense as the underlying process is inseparable. Trigonometric identities can be applied to Eq. (24) to express the Stokes wave in a time-varying form as [23]

$$S(t) = \frac{1}{2}a^{2}k + \alpha(t)\cos(\omega t + \phi(t)), \quad (k \ll 1)$$
with $\phi(t) = \tan^{-1}\frac{a^{2}k\sin\omega t/2}{a + a^{2}k\cos\omega t/2} \approx \frac{1}{2}ak\sin\omega t,$

$$\alpha(t) = \sqrt{a^{2} + (a^{2}k/2)^{2} + a^{3}k\cos\omega t} \approx a + \frac{1}{2}a^{2}k\cos\omega t.$$
(25)

From the phase function $\phi(t)$ in Eq. (25), the theoretical IF can be worked out as

IF =
$$\frac{1}{2\pi} (\omega + \dot{\phi}(t)) \approx \frac{1}{2\pi} \left(\omega + \frac{1}{2} ak\omega \cos \omega t \right)$$
. (26)

The intra-wave modulated IF in Eq. (26) is directly associated with the periodic harmonic distortion in the Stokes wave (i.e., the sharp crest and flat trough, see Fig. 4 (a)), which is a possible mechanism for the formation of rogue waves [38].

Different approaches are utilized to achieve the time-frequency analysis of the Stokes wave, as shown in Fig. 5. Fourier-based wavelet

analysis (see Fig. 5 (a)) provides results consistent with that in the power spectrum, and the wavelet-based SST technique (see Fig. 5 (b)) only sharpens the original distribution. The presence of noise undermines the effectiveness of the HHT method, making the spectrum unreadable (see Fig. 5 (c)). The time-frequency distribution obtained by the INCMD agrees well with the theoretical result (see Fig. 5 (d)), clearly capturing embedded intra-wave modulations as given in Eq. (26). Further Fourier analysis of the IF shows the 1X oscillating frequency (see Fig. 5 (e)), as Eq. (26) indicates. The signal decomposition results of the noisy signal by INCMD and VMD, respectively, are compared in Fig. 6. Owing to the wide-band demodulation framework of INCMD, the original Stokes wave is recovered with high accuracy (see Fig. 6 (a)), while the narrowband filter-bank-based VMD failed this task (see Fig. 6 (b)).

It has been demonstrated that a physically meaningful characterization of the Stokes wave can be achieved using the INCMD-based strategy. With the aid of such an approach, intra-wave modulation features extracted from milling responses similarly capture underlying dynamic processes, which will be demonstrated in simulated and experimental results in Sections 4 and 5.

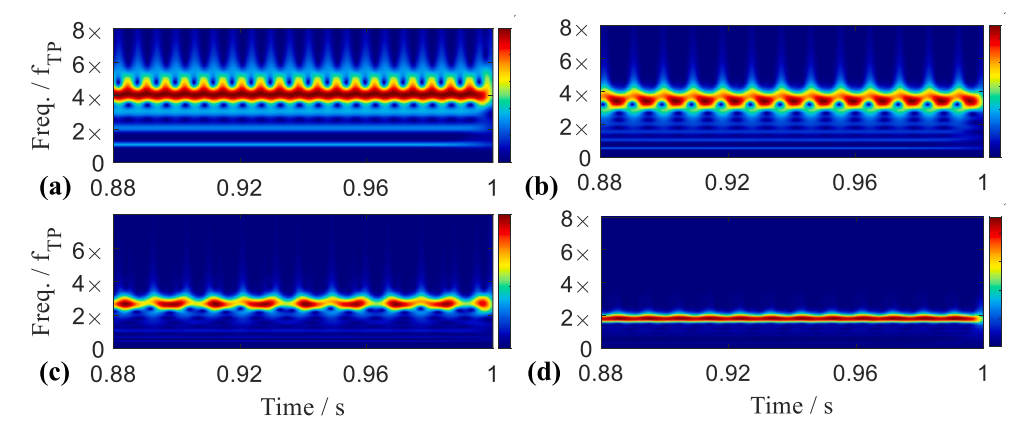


Fig. 8. Morlet scalograms of four sets of responses given in. (a) Stable cutting. (b) Pre-instability. (c) Chatter. (d) Post-instability.

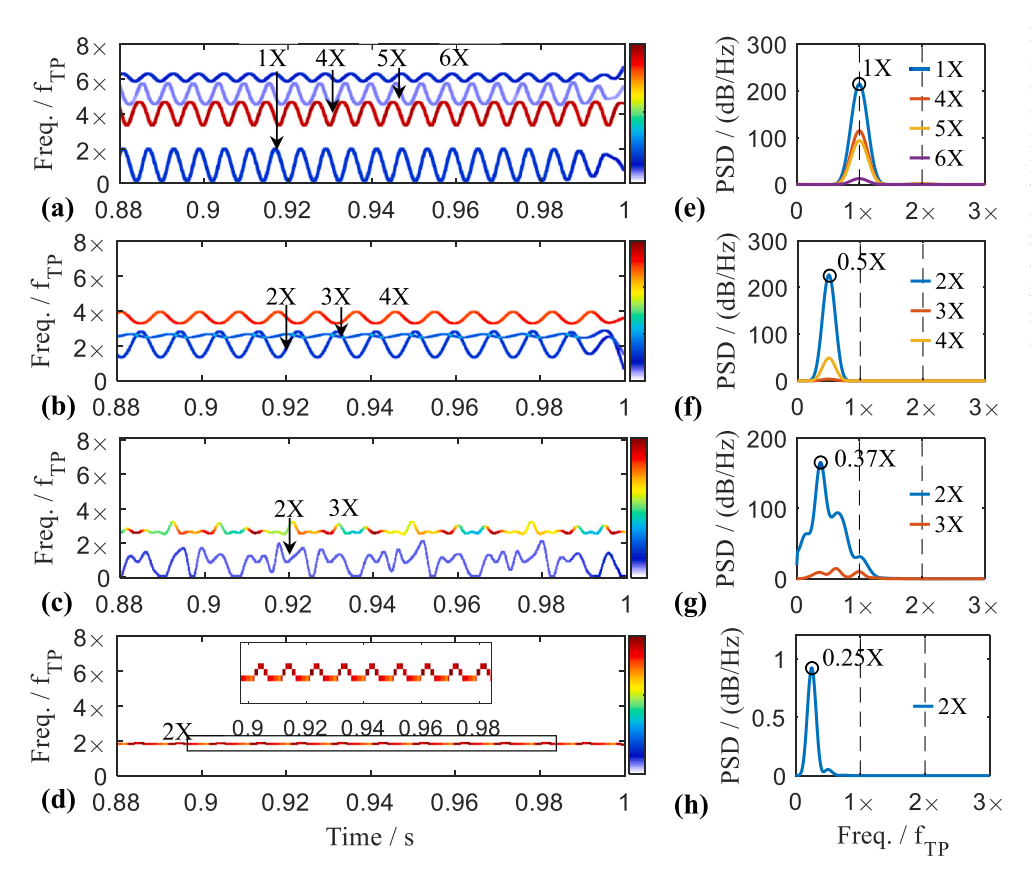


Fig. 9. Intra-wave modulations extracted from four sets of responses given in Fig. 7. (a, e) Stable cutting. (b, f) Pre-instability. (c, g) Chatter. (d, h) Post-instability. Left-side panels show INCMD spectra. Right-side panels show power spectra of IFs of intra-wave modulated modes (dashed black lines denote the tooth-passing frequency and its multiples, and different colors represent different modes). (For interpretation of the references to color in this figure legend, the reader is referred to the Web version of this article.)

4. Intra-wave modulated responses in milling processes

In this section, simulated milling responses are investigated with the assistance of the INCMD-based approach introduced in Section 3.2, with $\rho=1\times10^{-5},\,\mu=1\times10^{-5},$ and $\varepsilon=1\times10^{-8}$ (see Fig. 3) set for the INCMD if without a special note in following analyses. The system parameters remain the same as those used in Section 2.2, and the standard dde23 routine in MATLAB® is employed. We consider four cases mentioned in Section 2.2: stable cutting, pre-instability, chatter, and post-instability, which are denoted as A, B, C, and D, respectively, in the stability lobe (see Fig. 2 (a)).

The basic characterization of the studied tool vibrations is shown in Fig. 7. The temporal waveforms (see Fig. 7 (a, b, c, d)) demonstrate a set of responses with increasing amplitude and gradually more severe

shock. The periodic-1, periodic-2, quasi-periodic, and periodic-4 properties of tool motions are revealed in the phase portraits (see Fig. 7 (i, j, k, l)). Fig. 7 (e, f, g, h) shows the power spectra with the prominent components marked, the structures of which are in agreement with the theoretical predictions expressed in Eq. (8). Such frequency-domain descriptions are, however, incomprehensible from a physical point of view. Wavelet analysis is applied for a time-frequency description, as shown in Fig. 8. Besides the information in the power spectra, the frequency oscillations, though vaguely captured, can be observed in the Morlet scalograms. Moreover, the oscillation pattern changes as the cutting state transforms.

To ascertain the existence of all the above phenomena and elucidate the relationship between them, the intra-wave modulation features of four sets of responses are extracted and shown in Fig. 9. We discuss the

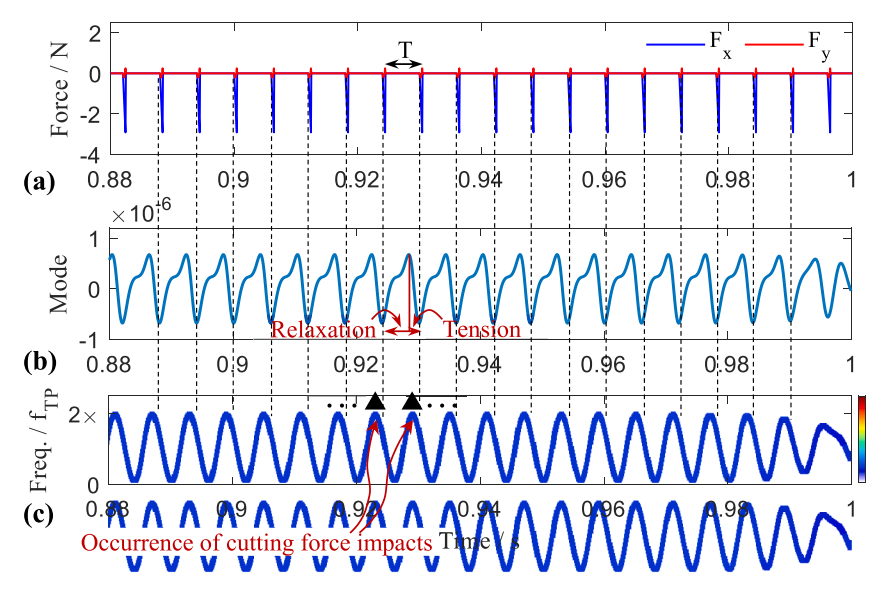


Fig. 10. Stiffening effect in intermittent milling processes. (a) Simulated cutting force under stable cutting. (b) 1X temporal mode extracted from the stable cutting response using the INCMD. (c) Close-up view of Fig. 9 (a) corresponding to the IF of the 1X mode.

results next.

4.1. Stable cutting

From the stable cutting response, four modes are extracted, the IFs of which oscillate sinusoidally around 1X, 4X, 5X, and 6X, respectively (see Fig. 9 (a)). Fourier analysis of the four IFs indicates a unified modulating frequency at 1X. This phenomenon implies the synchronous fluctuation of the transient vibrating frequency, which results from the stiffening effect [30], a dynamic process led by periodic cutting force impacts. Note that although the stiffening effect is discussed considering the rotor-to-stator rubbing system in Ref. [30], this phenomenon is common in intermittent milling as the workpiece and tool act as the stator and rotor, respectively, to some degree. As stated in Ref. [30], "the interaction between the rotor and stator equals to the addition of a transient support to the rotor, the transient stiffness of the system increases"; the periodic engagement between the tool and the workpiece causes periodic time-varying stiffness, and thus leads to oscillating IFs. The stiffening effect can also be observed in the cracked rotor [39] and cracked beam [40] systems, another two well-known impact systems with time-varying stiffness.

Such a physical interpretation is verified further in Fig. 10. The extracted 1X temporal mode (see Fig. 10 (b)) undergoes a *relaxation oscillation* [41] in which the *tension* is caused by the interaction between the tool and the workpiece, and *relaxation* occurs during the free vibration of the tool. The cutting force impact is accompanied by the peak of the oscillating IF, as shown in Fig. 10 (a, c), demonstrating the stiffening effect.

Substituting two essential parameters, the frequency center f_{base} and the modulation frequency f_{FM} , into the expanded mode in Eq. (12), the spectral set can be obtained as

which constitute the f_{TP} (i.e., 1X) and its multiples, accounting for the

real spectral distribution (see Fig. 7 (e)).

4.2. Pre-instability: periodic-2 motion

Preceding the quasi-periodic chatter, periodic-2 motion is generally not regarded as cutting instability because it still belongs to controllable periodic vibrations [35]. However, it is unstable in the sense of dynamical systems because it originates from the flip bifurcation of the initial periodic-1 motion. Periodic-2 motion, therefore, acts as a pre-instability.

Although the modulation pattern in Fig. 9 (b) resembles that in Fig. 9 (a), the modulation frequency has switched to 0.5X. The impact-induced stiffening effect has developed into a non-synchronous yet periodic process that occurs once in every two rotating periods. Applying a similar substitution, the spectral set can be obtained as

$$f_{p-2} = \{ [(2\times) + n_1(0.5\times)], [(3\times) + n_2(0.5\times)], [(4\times) + n_3(0.5\times)] \} (f_{TP}), n_m = 0, \pm 1, \pm 2, \dots; m = 1, 2, 3,$$
(28)

which leads to the rise of half-order harmonics between adjacent integer-order harmonics, as shown in Fig. 7 (f).

4.3. Quasi-periodic chatter

Quasi-periodic chatter is a notorious instability phenomenon that results from the Neimark-Sacker bifurcation of the periodic motion. Essentially different from the two cases discussed above, the IFs here exhibit a seemingly random oscillation (see Fig. 9 (c)). The power spectrum of IFs, presenting a broad band though, shows a noticeable peak at 0.37X, which is the corresponding theoretical chatter frequency (see Fig. 2 (b)). Irrational multiples exist in the spectrum as

$$f_{stable} = \{ [(1 \times) + n_1(1 \times)], [(4 \times) + n_2(1 \times)], [(5 \times) + n_3(1 \times)], [(6 \times) + n_4(1 \times)] \} (f_{TP}),$$

$$n_m = 0, \pm 1, \pm 2, \dots; m = 1, 2, 3, 4.$$
(27)

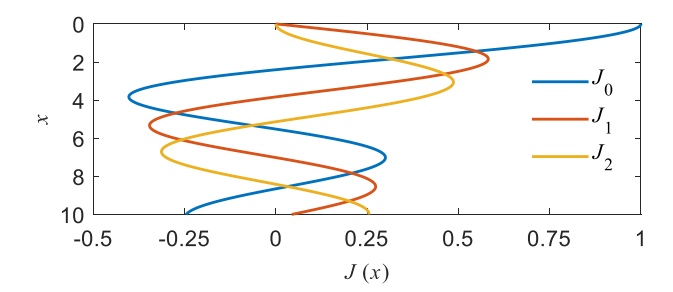


Fig. 11. Bessel functions for the first three orders of the first kind $(J_0 \sim J_2)$ [31].

$$f_{quasi} = \{ [(2 \times) + n_1(0.37 \times)], [(3 \times) + n_2(0.37 \times)] \} (f_{TP}), n_m = 0, \pm 1, \pm 2, \dots; m = 1, 2.$$
 (29)

Quasi-periodic engagements between the tool and workpiece bring about the tangled side bands given in Eq. (29), as shown in Fig. 7 (g).

4.4. Post-instability: periodic-n motion

As chatter develops, the periodic response may emerge again through the secondary flip bifurcation of quasi-periodic chatter [35], as shown in Fig. 7 (d). The modulation frequency at 0.25X (see Fig. 9 (h)) leads to the spectral distribution of the periodic-4 motion as

$$f_{p-4} = \{ [(2 \times) + n(0.25 \times)] \} (f_{TP}), \ n = 0, \pm 1, \pm 2, \cdots,$$
 (30)

which agrees with that shown in Fig. 7 (h). Such a mechanism can be generalized to periodic-n motion, the power spectrum of which would exhibit the 1/n-th order harmonics [42].

4.5. Discussions

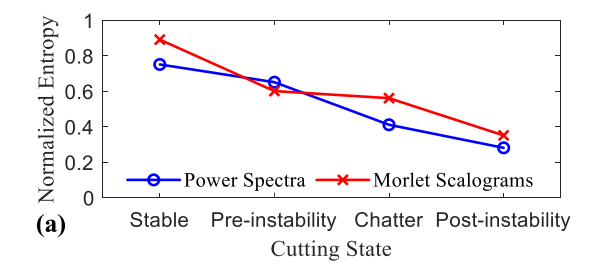
4.5.1. Energy concentration in chatter

In addition to the evolution of the modulation pattern discussed above, the number of extracted modes decreases as chatter becomes more severe (see Fig. 9 (a, b, c, d)). This phenomenon implies the concentration of energy, which has also been observed by Chen et al. [43] who used the Rényi entropy, and Cao et al. [44] who used the standard deviation to characterize the dispersion in the distribution of spectral sequences of the milling responses. According to these studies, the energy of vibration responses will be absorbed into a certain resonance band both in the frequency and time-frequency domains when chatter occurs.

We calculated the normalized Rényi entropy values [43] (see Appendix A for detailed formulas) of the power spectra (see Fig. 7 (e, f, g, h)) and Morlet scalograms (see Fig. 8) of four sets of simulated responses, and the results are shown in Fig. 12 (a). The decreasing entropy quantitatively describes the gathering energy in the frequency and time-frequency domains, which is consistent with the conclusions derived in Ref. [43]. As the greedy strategy is adopted in the INCMD algorithm (i.e., the extracted mode in each recursion takes away as much energy as possible within a certain bandwidth), the concentration of energy within a small bandwidth (see Fig. 12 (b)) naturally reduces the obtained modes, as mentioned in Section 3.2.

4.5.2. Physics of intra-wave modulation and consistency with spectral distribution

Because the series model Eqn (12) can be truncated, we expand the extracted mode $w_k(t)$ to the first three orders as



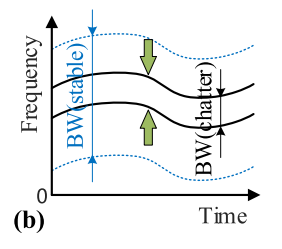


Fig. 12. Energy concentration when chatter occurs. (a) Normalized Rényi entropy values of power spectra and Morlet scalograms of four sets of simulated responses. (b) Energy concentration in time-frequency domain (where "BW" means "bandwidth").

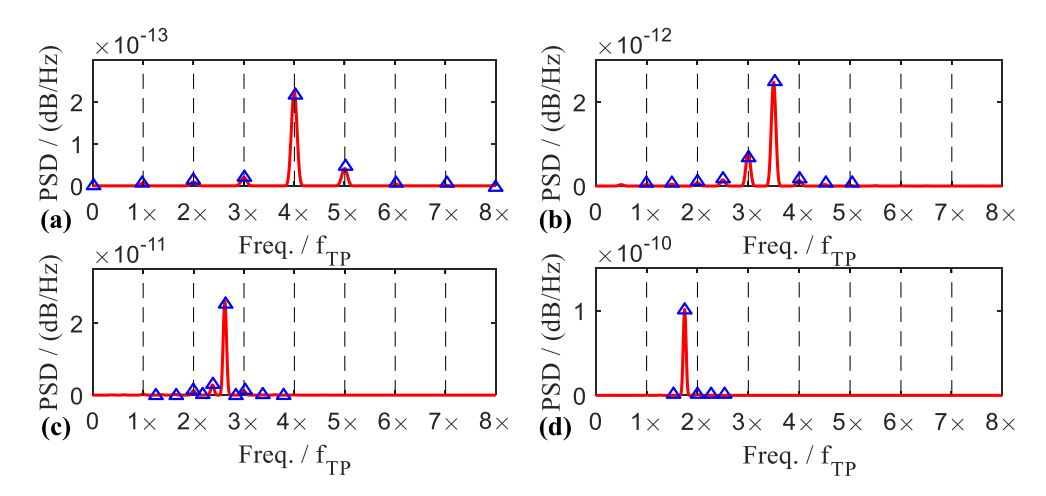


Fig. 13. Mathematical consistency between intra-wave modulations and spectral distributions. (a, b, c, d) correspond to four sets of responses given in Fig. 7, where red lines are the true power spectra of simulated responses as shown in Fig. 7 (e, f, g, h), while blue triangles denote the coefficients of harmonics obtained using the truncated model Eqb (31). (For interpretation of the references to color in this figure legend, the reader is referred to the Web version of this article.)

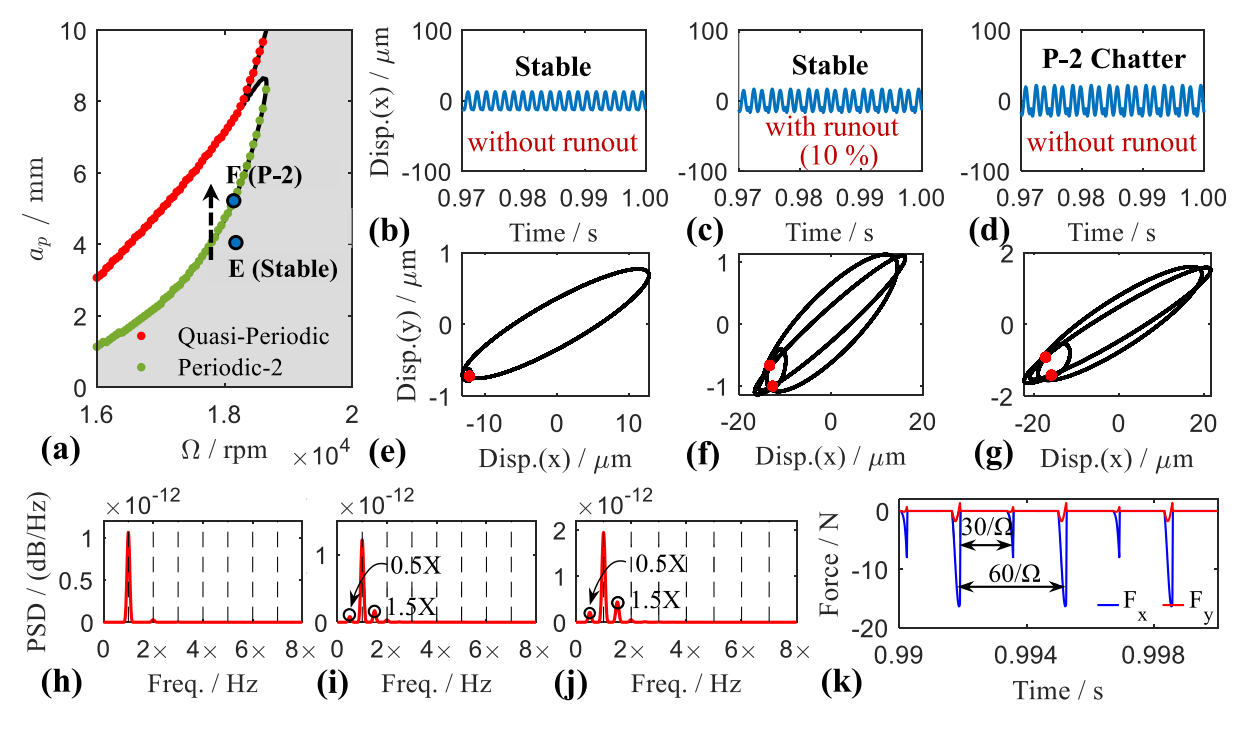


Fig. 14. Simulated tool vibrations considering the two-tooth tool. (a) Stability lobe. (b, c, d) Temporal waveforms. (e, f, g) Phase portraits. (h, i, j) Power spectra. (k) Cutting force. Three panels from the left to the right in (b, c, d), (e, f, g), and (h, i, j) correspond to the stable (marked with E in (a)), stable with runout at the 10% level, and P-2 chatter (marked with F in (a)) state, respectively, while (k) corresponds to the stable state with runout at the 10% level. Simulation duration is taken as 0–1 s and the steady-state during 0.97–1 s is truncated for analyses. Fig. 7 can be referred to for the meaning of other notations.

$$w_k(t) = \sum_{n=0,\pm 1,\pm 2} J_n(\varepsilon_{FM,k}) \left\{ a_k(t) \cos\left(2\pi \left(f_{base,k} + nf_{FM,k}\right)t + n\theta_k + \phi_k\right) \right\}, \quad (31)$$

where the Bessel functions $J_n(\cdot)_{n=0,1,2}$ of the first kind are shown in Fig. 11 (note that the relationship $J_{-n}(x)=(-1)^nJ_n(x)$ exists [31]), whose variation pattern is complex.

The truncated model Eqn (31) is essentially the superposition of a finite number of harmonics. In Sections 4.1–4.4, the oscillation parameters including the center frequency f_{base} and modulation frequency f_{FM} have been substituted into Eq. (12) to obtain the spectral set. In fact, all the descriptive constant parameters in Eq. (12) can be acquired after the intra-wave modulation analysis, as demonstrated in Section 3.2 (see

Fig. 3). By substituting the complete parameter set into Eq. (31), sampling the Bessel functions at specific values, and combining like terms, we can finally obtain four sets of harmonics corresponding to the vibration responses in Fig. 7. The coefficients of these harmonics are plotted in Fig. 13 with the true power spectra for comparison. Perfect matching can be observed between the spectral peaks obtained by two methods, which strongly demonstrates the mathematical rigor of the characterization using intra-wave modulations and its consistency with spectral distributions.

The classic Fourier transform expands the signal using a set of trigonometric bases that are linear and stationary. By contrast, nonlinear and nonstationary bases are adaptively selected in intra-wave

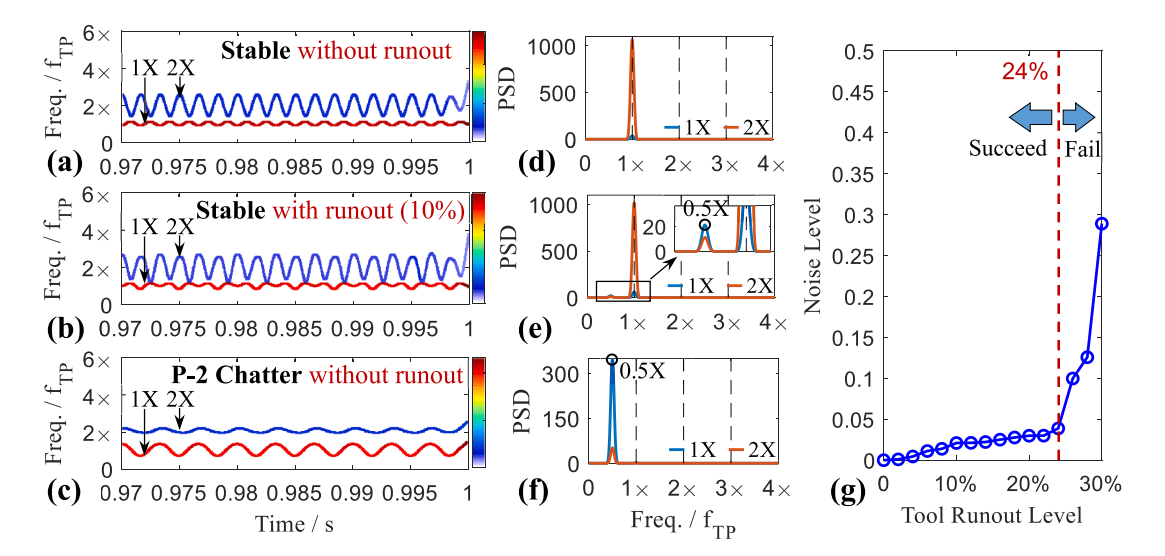


Fig. 15. Intra-wave modulation analyses of three sets of responses given in Fig. 14. (a, b, c) INCMD spectra. (d, e, f) Power spectra of IFs. (g) Resulting noise level versus the tool runout level.

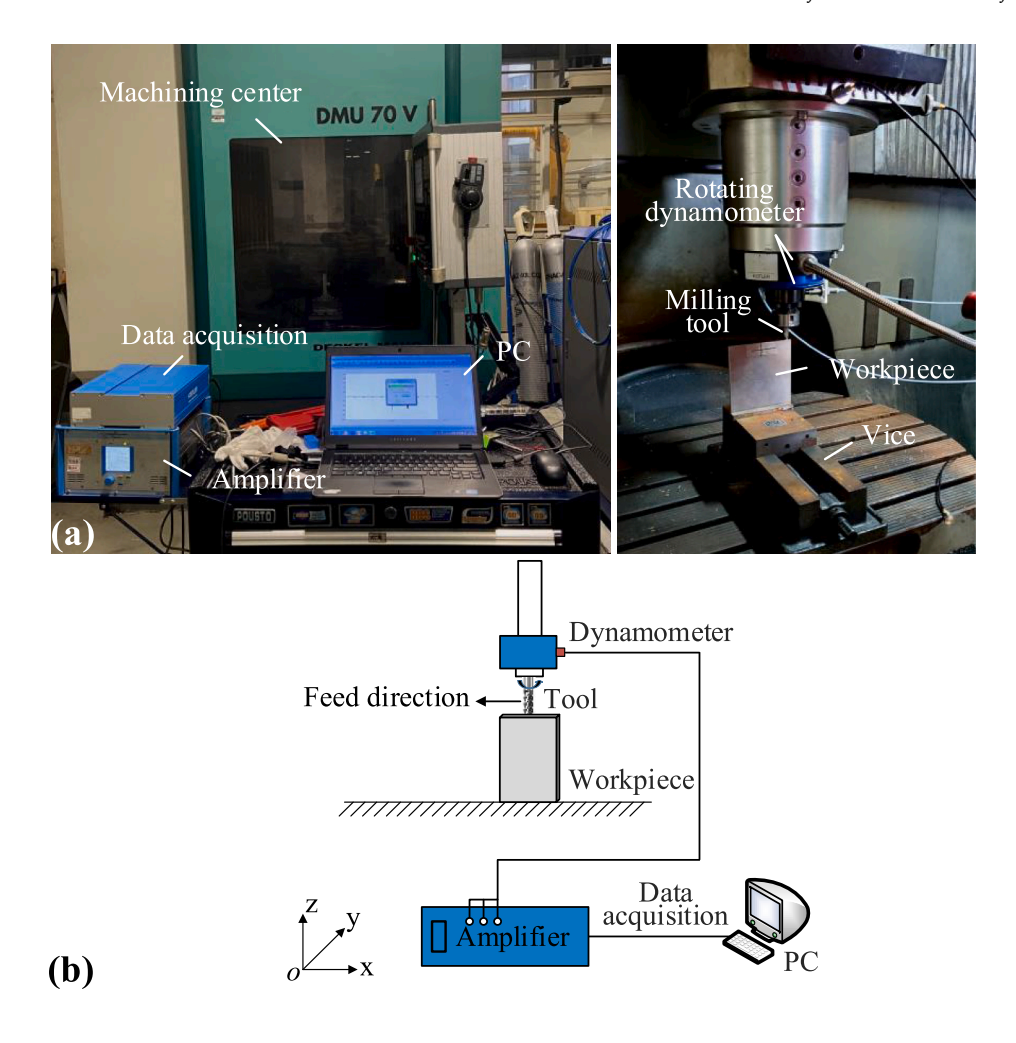


Fig. 16. Experimental setup of the milling system. (a) Picture. (b) Schematic.

modulation analyses. When processing the milling responses, the resulting bases are a series of parsimonious harmonic-like single modes, the IFs of which oscillate around the tooth-passing frequency, synchronized with intermittent cutting force impacts as demonstrated in Section 4.1. Some integer- and non-integer-order harmonics are embedded in the modulation features but do not arise explicitly as they do in the power spectra. Taking the case of stable cutting as an example, all six harmonics from 1X to 6X can be observed in the power spectrum (see Fig. 7 (e)), but only four intra-wave modulated modes centered on 1X, 4X, 5X, and 6X are extracted, as shown in Fig. 9 (a).

In other words, we can always obtain a sparse time-frequency representation of milling responses using intra-wave modulation analyses. Based on the discussion in Section 4.5.1, this comes as no surprise because the extracted modes will be as few as possible with greedy algorithms. From this viewpoint, these redundant harmonics do not exist physically because dynamical systems in nature can always be characterized with sparsity [45,46], as concluded by Huang when he employed the Hilbert spectrum to interpret the harmonic distortion of nonlinear Stokes waves [29] (note that this example is also given in Section 3.3).

4.5.3. Impact of tool runout on accuracy

In the simulations above, the tool teeth number is set as one to exclude the runout effect. In practice, tool runout is inevitable and could have an impact on identification accuracy when using the proposed method. Considering the two-tooth tool (i.e., N=2) with runout, besides the tooth-passing components, the spindle rotating frequency (i.e., 0.5X) and its multiples will arise in the power spectrum. As discussed in

Section 4.1–4.4, when quasi-periodic or periodic-n (n > 2) chatter occurs, the modulation frequency is less than 0.5X and thus "0.5X" can be regarded as the new "1X" [15]. However, when periodic-2 chatter occurs, the 0.5X, along with its multiples caused by the instability, will coincide with the same frequencies caused by the runout. Such problematic situations are discussed in detail here.

For simplicity, the milling model in Section 2.1 is still used, and the tool runout is described by a pair of imbalance factors because the chip load will be distributed unevenly on two teeth when runout exists [47]. Eq. (4) is modified as

$$\begin{cases}
F_{x,j}(t) = \rho_j \left(-F_{r,j}(t)\sin(\varphi_j(t)) - F_{t,j}(t)\cos(\varphi_j(t)) \right), \\
F_{y,j}(t) = \rho_j \left(-F_{r,j}(t)\cos(\varphi_j(t)) + F_{t,j}(t)\sin(\varphi_j(t)) \right),
\end{cases}$$
(32)

where all the elements other than the added weighting factors ρ_j remain unchanged. When the tool is perfectly symmetrical $\rho_1=\rho_2=1$, whereas $\rho_1\neq\rho_2$ when runout exists. The tool runout level is defined here as $(|\rho_1-\rho_2|)/(\rho_1+\rho_2)$, e.g., " $\rho_1=0.9$, $\rho_2=1.1$ " means the runout at the 10% level.

Because the runout at low levels barely affects the stability boundary [15], $\rho_1=\rho_2=1$ is set first, and semi-discretization is used to obtain the stability lobe in Fig. 14 (a). The stable cutting and periodic-2 chatter, marked with E ($\Omega=18\times10^3$ rpm, $a_p=4$ mm) and F ($\Omega=18\times10^3$ rpm, $a_p=5$ mm) in the lobe, respectively, are considered, and stable cutting with runout at the 10% level is also simulated. The temporal waveforms, phase portraits, and power spectra of the three sets of responses are shown in Fig. 14 (b, c, d), (e, f, g), and (h, i, j), respectively. The variation in the cutting force acting on two teeth due to runout is

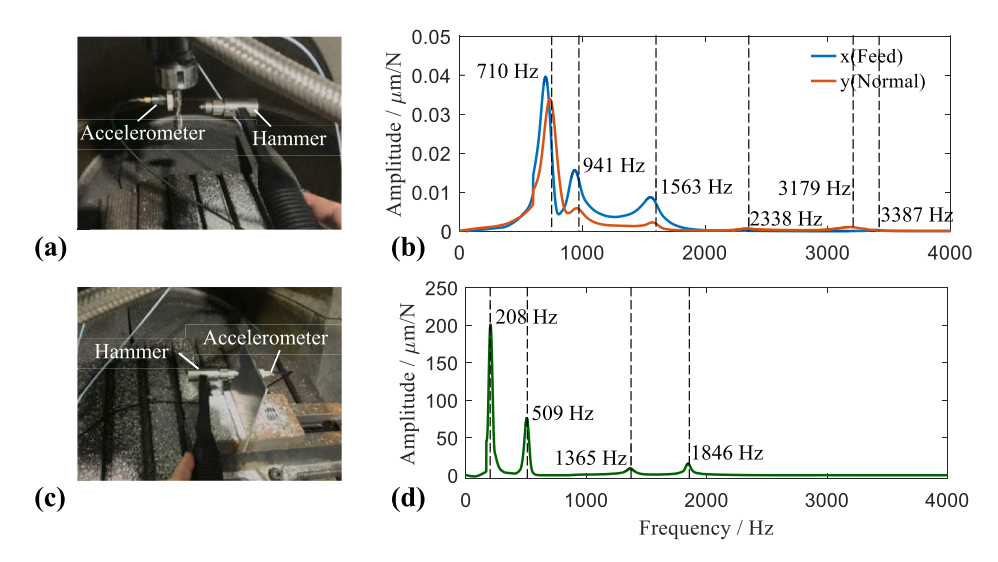


Fig. 17. Measured FRFs of the milling system. (a, b) Impact test for the tool (left) and the resulting FRF (right). (c, d) Impact test for the workpiece (left) and the resulting FRF (right).

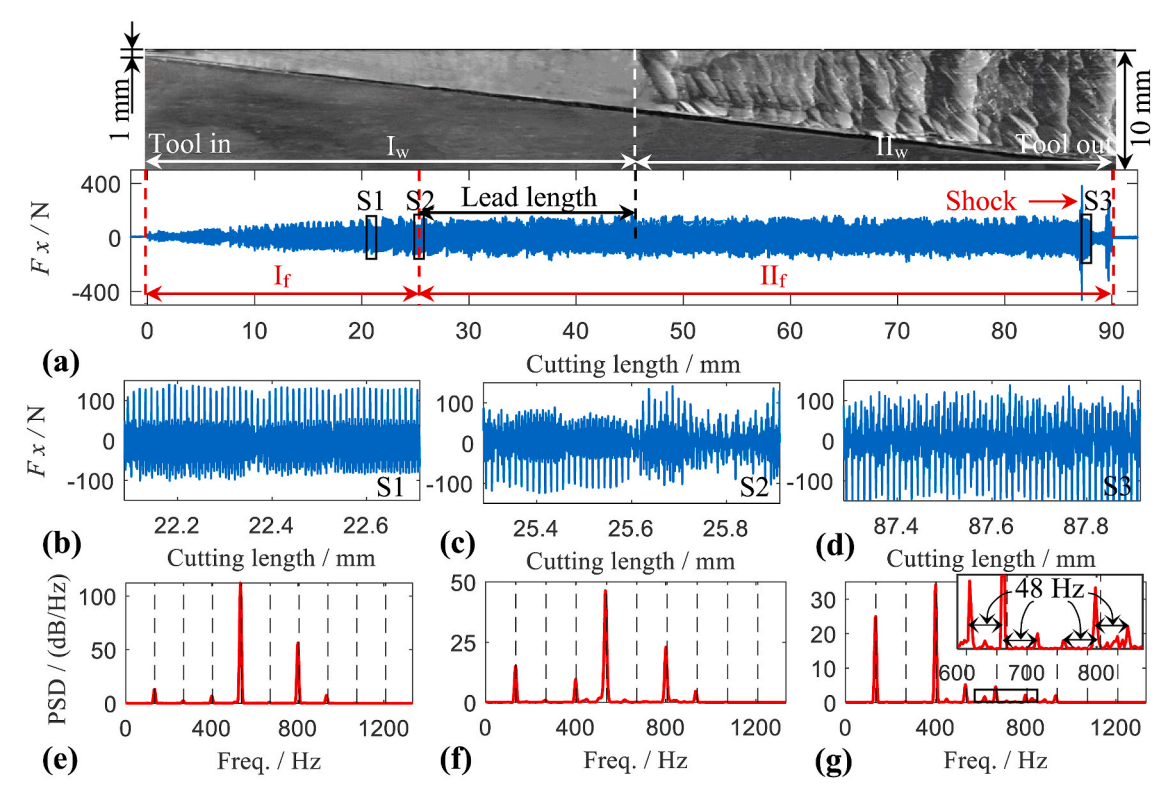


Fig. 18. The first set of experimental data (2% immersion ratio). (a) Milling force signal with the workpiece surface finish. (b, c, d) Three segments of the force signal with (e, f, g) their power spectra, corresponding to the S1, S2, and S3 windows marked in (a).

clearly shown in Fig. 14 (k), leading to a considerable amplitude at 0.5X and 1.5X frequencies and the split of the Poincaré attractor. As a result, periodic-2 chatter and stable cutting cannot be distinguished based on the power spectra or phase portraits.

The runout effects also disturb the intra-wave modulation analyses, but the resulting error could be negligible. As Fig. 15 (a, b, c) shows, the INCMD spectra under stable cutting are almost the same with and without runout. When runout exists, an extremely small spike can be observed at 0.5X in the power spectrum of IFs, whose amplitude is only 2% of that at 1X, whereas for periodic-2 chatter, IFs oscillate purely at 0.5X, as concluded in Section 4.2.

Considering the spike at 0.5X as the unwanted noise and defining the

noise level as the ratio of the spike amplitude to the 1X amplitude in the PSD of IFs (the highest among multiple peaks is taken), we conduct tests at different tool runout levels. The results are shown in Fig. 15 (g). An acceptable threshold of the runout level at 24% is obtained, before which the noise remains weak. Although only the two-tooth case is discussed here, the coincidence between chatter frequencies and runout frequencies appears in any case with an even number of tool teeth. Therefore, the conclusions above can be generalized.

Among the intricate spectral components, critical indicative information could be submerged and hidden. With the aid of intra-wave modulation analyses, weak and fragile dynamic features embedded in milling responses are extracted and amplified, which helps to detect

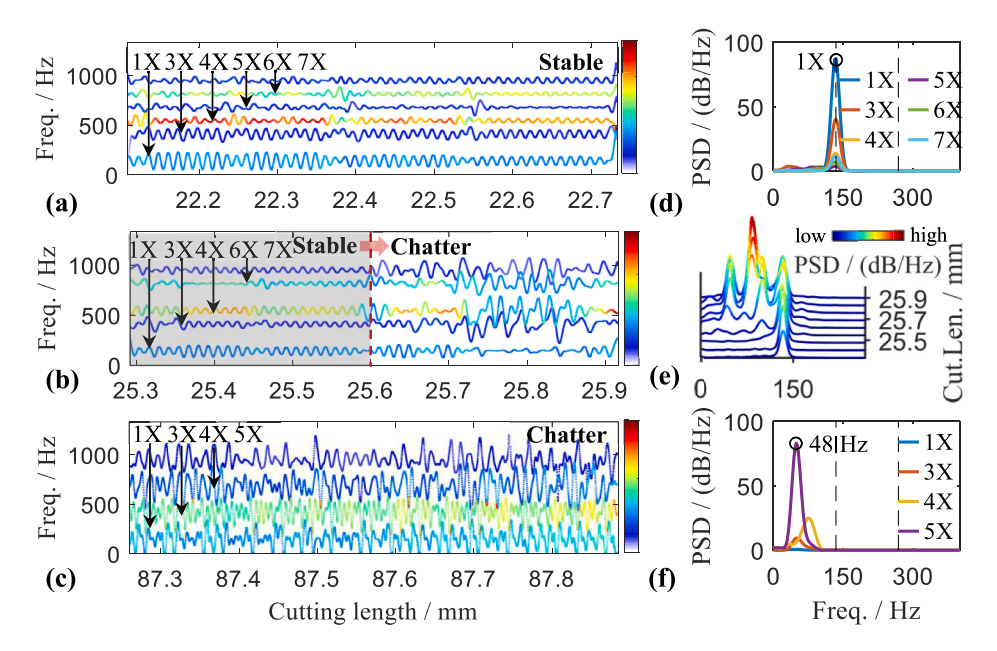


Fig. 19. Intra-wave modulations extracted from three segments of the first set of experimental data. (a, d), (b, e), and (c, f) here correspond to (b, c, d) in Fig. 18 respectively. Left-side panels show INCMD spectra. Right-side panels show power spectra of IFs of intra-wave modulated modes (in (d) and (f), different colors represent different modes; while in (e) is a cascade plot where the spectrum at each cutting length is the superposition of that of all modes). (For interpretation of the references to color in this figure legend, the reader is referred to the Web version of this article.)

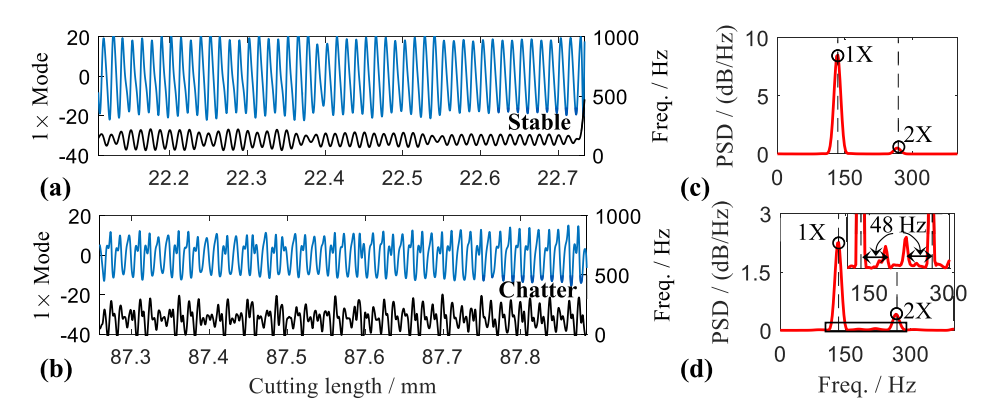


Fig. 20. The 1X modes extracted from the (a, c) S1 and (b, d) S3 segments of the first set of experimental data (see Fig. 18 (a)). Left-side panels show temporal modes (blue lines) with their IFs (black lines). Right-side panels show power spectra of modes. (For interpretation of the references to color in this figure legend, the reader is referred to the Web version of this article.)

chatter in a premature phase. We validate this experimentally in Section $\mathbf{5}$

5. Experimental verification

5.1. Setup

This section describes the dedicated experiments that were conducted to verify the conclusions obtained in Section 4. Fig. 16 shows the experimental setup that corresponds to the schematic in Fig. 1. Milling tests were performed on a five-axis DMU 70V vertical machining center with a spindle speed of up to 10,000 rpm. The cantilevered aluminum workpiece was clamped in a vice with the free-end dimension of $100\times100\times3$ mm. One side of the free end was up-milled by a high-speed-steel two-tooth tool with a diameter of 10 mm, where the second tooth was ground off. Because the force signal is subjected to the least interference while the fidelity of measured displacements and accelerations are greatly affected by the placement of sensors [11], the milling force is analyzed here. The Kistler® 9170A rotating dynamometer, which has the cutting frequency of 2 kHz, was used to obtain milling forces in the feed and its normal directions. All measured data were collected using an acquisition device at a sampling frequency of 10 kHz.

Standard impact tests were conducted to measure the structural

resonance, and the resulting frequency response functions (FRFs) are shown in Fig. 17. In the cutting experiments, the spindle speed was fixed at $8000 \, \text{rpm}$ and the feed was fixed at $0.0125 \, \text{mm/tooth.}^2$ Tool cuts were made at the free end of the workpiece in a 90 mm long track centered with respect to the side of the plate. The axial cutting depth increased uniformly from 1 mm to 10 mm. Two sets of tests with radial cutting depths of $0.2 \, \text{mm}$ and $0.5 \, \text{mm}$ (i.e., immersion ratios as 2% and 5%, respectively) were conducted.

5.2. Results

The first set of experimental data is shown in Fig. 18 (a). The force signal in the feed direction (i.e. F_x) and the surface finish of the work-piece are presented. Visible chatter marks did not emerge until half of the cutting length (i.e., 5.5 mm axial depth), dividing the machined area into I_w and II_w , accordingly. The cutting force, however, exhibits no drastic changes in amplitude throughout, except for a conspicuous shock

² Note that a small feed rate was set since the stiffness of the workpiece used here is too low. The tool edge chipping emerges soon if a normal feed rate is set. In practical engineering, the method proposed in this paper works under normal feed rates larger than 0.1 mm/tooth.

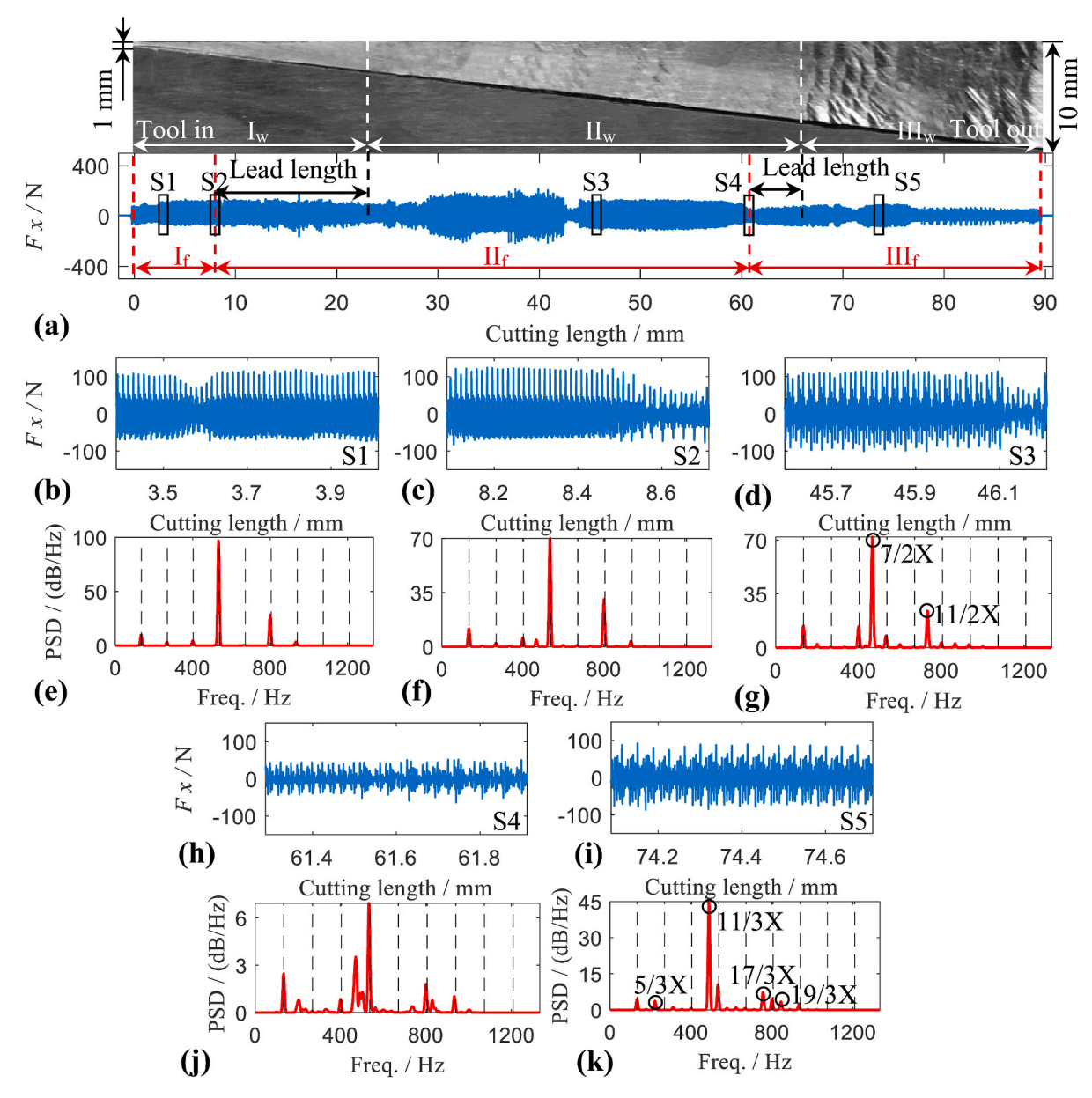


Fig. 21. The second set of experimental data (5% immersion ratio). (a) Milling force signal and the workpiece surface finish. (b, c, d, h, i) Five segments of the force signal with (e, f, g, j, k) their power spectra, corresponding to the S1, S2, S3, S4, and S5 windows marked in (a).

near the end of cutting. Using the INCMD spectrum, intra-wave modulations of the response are monitored using a sliding window with a size of 50 spindle periods. A switch in the modulation pattern is captured at a cutting length of 25.6 mm, signifying two phases $\rm I_f$ and $\rm II_f$ in the response. Two window segments S1 and S3 in phase $\rm I_f$, $\rm II_f$, and the transition segment S2 across them are given in Fig. 18 (b, d, c), respectively. Valuable information can hardly be extracted from their power spectra because the tooth-passing components dominate while the non-tooth-passing components are too weak to be distinguished from noise.

Extracted intra-wave modulation features (see Fig. 19) demonstrate three distinct processes. The incipient segment S1 consists of six modes whose IFs oscillate at the 1X frequency (see Fig. 19 (a)), indicating stable cutting as discussed in Sub-section 4.1. The above process lasts until the periodicity of IFs ceases at the 25.6 mm cutting length. The cascade power spectrum of IFs illustrates a transition from stable cutting to quasi-periodic chatter, where irrational multiples of the 1X arise progressively (see Fig. 19 (e)).

With a shock in the force signal at a cutting length of approximately 87 mm (see Fig. 18 (a)), the chatter becomes fully developed. As Fig. 19 (c) shows, pseudo-randomly fluctuating IFs embed chatter frequency information at 48 Hz, which can be verified by weak sidebands in the power spectrum of the response (see Fig. 18 (g)). Such a transformation also manifests itself in the extracted 1X modes. While power spectra hardly capture the differences (see Fig. 20 (c, d)), relaxation oscillation (see Fig. 20 (a, b)) and intra-wave modulation patterns clearly show the distinctions between the two modes. In addition, the number of extracted modes decreases when chatter becomes more severe, as concluded in Section 4. Note that the switch of the modulation pattern emerges far earlier than visible chatter marks do (see Fig. 18 (a)). Such switches, in this respect, are able to predict, rather than just indicate, the coming of the new cutting state.

With the increase in the immersion ratio, the second set of experimental data originates from a more complicated process, as shown in Fig. 21 (a). Slight chatter marks appear first before the severe final ones, separating the machined area into three parts, I_w , II_w , and III_w .

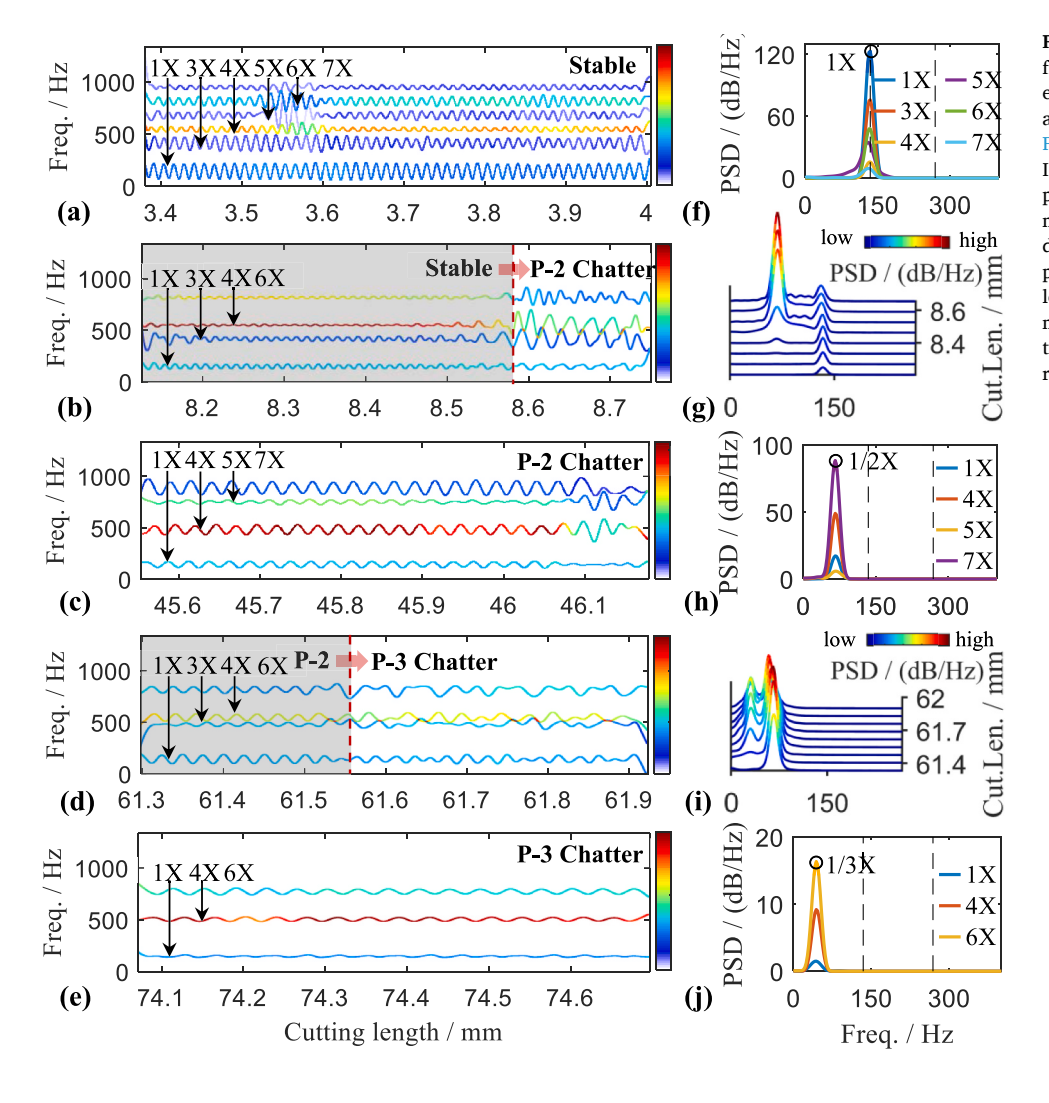


Fig. 22. Intra-wave modulations extracted from five segments of the second set of experimental data. (a, f), (b, g), (c, h), (d, i), and (e, j) here correspond to (b, c, d, h, i) in Fig. 21 respectively. Left-side panels show INCMD spectra. Right-side panels show power spectra of IFs of intra-wave modulated modes (in (f, h, j) different colors represent different modes; while in (g, i) are cascade plots where the spectrum at each cutting length is the superposition of that of all modes). (For interpretation of the references to color in this figure legend, the reader is referred to the Web version of this article.)

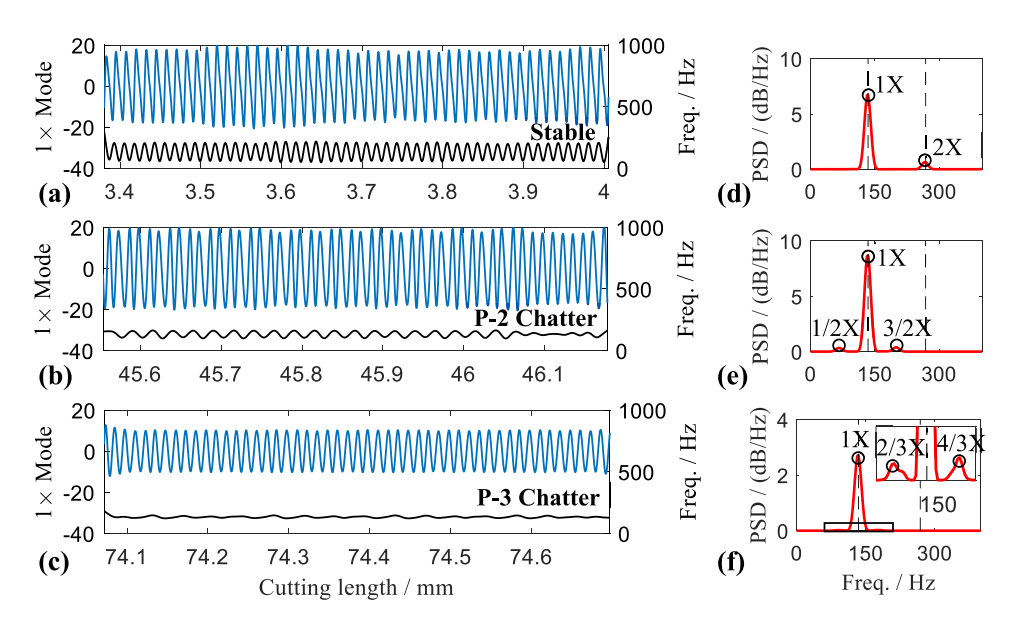


Fig. 23. The 1X modes extracted from the (a, d) S1, (b, e) S3, and (c, f) S5 segments of the second set of experimental data (see Fig. 21 (a)). Left-side panels show temporal modes (blue lines) with their IFs (black lines). Right-side panels show power spectra of modes. (For interpretation of the references to color in this figure legend, the reader is referred to the Web version of this article.)

Perplexing fluctuations in amplitude exist throughout the milling force though, intra-wave modulation analysis is still applied to comprehend the underlying process. Two switches of the modulation pattern are captured, suggesting three phases I_f , II_f , and III_f in the response. Characteristic fractional harmonics in the power spectra of the developed stages S3 and S5 in phase II_f , III_f (see Fig. 21 (g, k)) reveal an ostensibly periodic-2 and periodic-3 process, respectively, which is, however, to be confirmed.

As Fig. 22 illustrates, the extraction of intra-wave modulation features eliminates the need to interpret intricate power spectra. During the first transition segment S2, the periodicity of oscillating IFs holds throughout, but the period itself elongates at approximately 8.6 mm of the cutting length (see Fig. 22 (b)). A transition from stable cutting to periodic-2 chatter is clearly captured in the cascade power spectrum of IFs, while such time-varying features are totally lost in the power spectrum of the original response (see Fig. 21 (f)). A similar transition from periodic-2 to periodic-3 chatter can be observed in segment S4 (see Fig. 22 (d)), where the period of IFs elongates again at approximately 61.6 mm of the cutting length, accompanied by the rise of the 1/3-order sub-harmonic in the power spectrum of IFs (see Fig. 22 (i)).

In contrast to the first set of experimental data, the periodicity of the response is maintained throughout the second set, which can also be observed in the extracted 1X modes (see Fig. 23). In such a case, the relaxation oscillation forms of the three modes can be barely distinguished, whereas the intra-wave modulation patterns are of great help in identifying the cutting states. Similarly, periodic-2 and periodic-3 motions precede the emergence of slight and severe chatter marks (see Fig. 21 (a)), respectively, verifying the pre- and post-instability attributes of these two types of responses, as discussed in Sub-sections 4.2 and 4.4. In addition, as the chatter intensifies, a decrease in the number of extracted modes can be observed in Fig. 22.

Moreover, from the measured FRFs in Fig. 17 and the power spectra under chatter in Figs. 18 and 21, it can be observed that chatter in the two experiments originates from the tool resonance (700 Hz) and workpiece resonance (500 Hz), respectively. Note that such a priori information is not needed in intra-wave modulation analyses because the derived conclusions in Section 4 are general and not related to the detailed system dynamics.

6. Conclusions

This study focuses on the intra-wave modulation phenomenon in milling processes. A multicomponent signal in which each mode owns a time-varying IF and IA is provided to model the milling responses. Simple post-processing techniques are combined with INCMD, a recently proposed approach for analyzing complex dynamic responses, to extract the distribution and oscillation features of the model signal in the time-frequency domain. With the aid of such a strategy, intra-wave modulations in the noisy Stokes wave, which is subjected to periodic harmonic distortion, are accurately extracted. Using this approach, the intra-wave modulation patterns of milling responses and the corresponding intrinsic physical processes under different cutting states are investigated through dynamic simulations and experimental verification. In addition, the internal relationship between the modulation patterns, spectral distributions, and dynamical bifurcations is established. Some important conclusions are summarized as follows:

- (1) In stable cutting, infinite harmonic processes do not exist but are induced by a limited number of intra-wave modulated modes. The IFs of these modes are centered on the tooth-passing frequency and its multiples (i.e., nX) and are modulated at exactly the tooth-passing frequency (i.e., 1X). Such phenomena result from the stiffening effect caused by intermittent cutting impacts, also accounting for the relaxation oscillation of temporal modes.
- (2) Milling instability is accompanied only by the switch of the modulation frequency while the distribution characteristics remain unchanged (i.e., IFs of modes still oscillate around the nX when chatter occurs), demonstrating the physical meaninglessness of the non-integer-order harmonics arising in the power spectra. Spurious and intricate spectral components can be mathematically interpreted by the series expansion of intra-wave modulated responses using Bessel functions.
- (3) The modulation frequencies under different cutting states are distinct. The incipient periodic-1 motion, the subsequent period-2 motion caused by the flip bifurcation, the later quasi-periodic motion originating from the Neimark-Sacker bifurcation, and the final periodic-n motion led by the secondary flip bifurcation, which indicate the stable cutting, pre-instability, chatter, and post-instability, respectively, are characterized by the modulation frequency at 1X, 1/2X, λ X (λ denotes an irrational number between 0 and 1), and 1/nX. These frequencies are equal to the chatter frequencies derived in bifurcation calculations based on the Floquet theory.

Moreover, it has been observed in experiments that the switch of the modulation pattern, which remains noticeable despite perturbation of noise, emerges far earlier than visible chatter marks do. In this regard, such switches can not only characterize but also predict the new cutting state; that is, chatter can be detected in a premature phase, demonstrating the superiority of such a cutting state indicator.

Complexity in industrial processes necessitates the introduction of physically meaningful characterizations to understand intrinsic dynamics. Intra-wave modulation analyses help mitigate the complexity of milling responses, and thus can be expected to further provide new insights into the dynamics and control in addition to condition monitoring of milling systems, which is our future work.

CRediT author statement

Guowei Tu: Data curation, Investigation, and Writing - original draft preparation. **Xingjian Dong:** Validation, Funding acquisition and Project administration. **Chao Qian:** Investigation and Data curation. **Shiqian Chen:** Methodology, Software and Writing - review & editing. **Lan Hu:** Visualization and Funding acquisition. **Zhike Peng:** Conceptualization, Supervision, and Resources.

Declaration of competing interest

The authors declare that they have no known competing financial interests or personal relationships that could have appeared to influence the work reported in this paper.

Acknowledgments

This work was supported by the National Natural Science Foundation of China [grant number 11872243] and the National Science and Technology Major Project of the Ministry of Science and Technology of China [grant number 2019ZX04025001]. The authors thank Dr. Baoxuan Zhao and Mr. Jiawei He for generous help in the conduction of

³ Although the signal features embedded in workpiece vibrations also exist in tool vibrations because of the coupling of the sub-systems [33], the tool-side vibration will not be very intense when chatter originates from the workpiece resonance generally. While in this study the weak chatter features can be magnified using intra-wave modulation analyses, in practical engineering, it would be better to monitor workpiece-side vibrations to detect chatter in time when the stiffness of the workpiece is much smaller than that of the tool.

experiments. They also thank Mr. Lei Zhang for insightful suggestions for improving the construction of this manuscript and his

encouragement, as always.

Appendix A. Calculation of Rényi entropy

The calculation of the normalized Rényi entropy [43] index is detailed in this section.

Considering the spectral amplitude sequence of the milling response as $\{X(k),\ k=1,2,\cdots,N\}$, the energy-based normalization can be applied to obtain a new sequence as

$$Y(k) = \frac{X(k)}{\sum_{i=1}^{N} X(k)},\tag{A.1}$$

where Y(k) ranges between 0 and 1, and $\sum_{k} Y(k) = 1$.

Recall that the Rényi entropy parameterized by α is defined as

$$H_{\alpha}(P) = \frac{1}{1 - \alpha} \log_2 \frac{\sum_{i=1}^{M} (P_i)^{\alpha}}{\sum_{i=1}^{M} P_i}, \ \alpha > 0, \ \alpha \neq 1,$$
(A.2)

where $\{P(i), i = 1, 2, \dots, M\}$ is the complete probability set of a random event. Eqn (A.2) can be generalized to characterize the energy distribution of milling responses in the frequency domain as (α is set as 3 following that in Ref. [43])

$$H_3(Y) = \frac{1}{1-3} \log_2 \frac{\sum_{k=1}^{N} (Y_k)^3}{\sum_{k=1}^{N} Y_k} = -\frac{1}{2} \log_2 \sum_{k=1}^{N} (Y_k)^3.$$
(A.3)

The index $H_3(Y)$ is normalized further to confine the value to be within the interval [0, 1] and independent of the data length as

$$RE(Y) = \frac{H_3(Y)}{\log_2 N} = -\frac{1}{2} \log_N \sum_{k=1}^N (Y(k))^3.$$
(A.4)

When dealing with two-dimensional spectra such as the Morlet scalograms shown in Fig. 8 in the main text, the amplitude data distributed in the time-frequency mesh plane are extracted and treated as a one-dimensional sequence. Then, the Rényi entropy can also be calculated using the formula Eqn (A.4).

The index RE(Y) is a dimensionless indicator, the value of which will reach the maximum when the spectral data are distributed evenly, that is, RE(Y) = 1 if and only if $Y(1) = Y(2) = \cdots = Y(N) = 1/N$. When the energy of the response gathers around a certain frequency band, that is, a few values are extremely large while others are kept at a low level, the index RE(Y) will become small.

References

- G. Quintana, J. Ciurana, Chatter in machining processes: a review, Int. J. Mach. Tool Manufact. 51 (2011) 363–376, https://doi.org/10.1016/j. ijmachtools.2011.01.001.
- [2] M. Eynian, In-process identification of modal parameters using dimensionless relationships in milling chatter, Int. J. Mach. Tool Manufact. 143 (2019) 49–62, https://doi.org/10.1016/j.jimachtools.2019.04.003.
- [3] G. Totis, M. Sortino, Polynomial Chaos-Kriging approaches for an efficient probabilistic chatter prediction in milling, Int. J. Mach. Tool Manufact. 157 (2020) 103610, https://doi.org/10.1016/j.ijmachtools.2020.103610.
- [4] D. Li, H. Cao, J. Liu, X. Zhang, X. Chen, Milling chatter control based on asymmetric stiffness, Int. J. Mach. Tool Manufact. 147 (2019) 103458, https://doi. org/10.1016/j.jimachtools.2019. 103458.
- [5] X.J. Zhang, C.H. Xiong, Y. Ding, M.J. Feng, Y. Lun Xiong, Milling stability analysis with simultaneously considering the structural mode coupling effect and regenerative effect, Int. J. Mach. Tool Manufact. 53 (2012) 127–140, https://doi. org/10.1016/j.ijmachtools. 2011.10.004.
- [6] B. Balachandran, Nonlinear dynamics of milling processes, Philos. Trans. R. Soc. London. Ser. A Math. Phys. Eng. Sci. 359 (2001) 793–819, https://doi.org/ 10.1098/rsta.2000.0755.
- [7] S. Seguy, G. Dessein, L. Arnaud, Surface roughness variation of thin wall milling, related to modal interactions, Int. J. Mach. Tool Manufact. 48 (2008) 261–274, https://doi.org/10.1016/j.ijmachtools.2007.09.005.
- [8] E. Budak, Y. Altintas, Analytical prediction of chatter stability in milling—Part I: general formulation, J. Dyn. Syst. Meas. Contr. 120 (1998) 22–30, https://doi.org/ 10.1115/1.2901317
- [9] T. Insperger, G. Stépán, Updated semi-discretization method for periodic delaydifferential equations with discrete delay, Int. J. Numer. Methods Eng. 61 (2004) 117–141, https://doi.org/10.1002/nme.1061.

- [10] P. Huang, J. Li, J. Sun, J. Zhou, Vibration analysis in milling titanium alloy based on signal processing of cutting force, Int. J. Adv. Manuf. Technol. 64 (2013) 613–621, https://doi.org/10.1007/s00170-012-4039-x.
- [11] E. Kuljanic, M. Sortino, G. Totis, Multisensor approaches for chatter detection in milling, J. Sound Vib. 312 (2008) 672–693, https://doi.org/10.1016/j. isv 2007.11.006
- [12] H. Caliskan, Z.M. Kilic, Y. Altintas, On-line energy-based milling chatter detection, J. Manuf. Sci. Eng. 140 (2018) 1–12, https://doi.org/10.1115/1.4040617.
- 13] T. Delio, J. Tlusty, S. Smith, Use of audio signals for chatter detection and control, J. Eng. Ind. 114 (1992) 146–157, https://doi.org/10.1115/1.2899767.
- [14] T. Insperger, G. Stépán, P. Bayly, B. Mann, Multiple chatter frequencies in milling processes, J. Sound Vib. 262 (2003) 333–345, https://doi.org/10.1016/S0022-460X(02)01131-8
- [15] T. Insperger, B.P. Mann, T. Surmann, G. Stépán, On the chatter frequencies of milling processes with runout, Int. J. Mach. Tool Manufact. 48 (2008) 1081–1089, https://doi.org/10.1016/j.ijmachtools.2008.02.002.
- [16] Z. Dombovari, A. Iglesias, M. Zatarain, T. Insperger, Prediction of multiple dominant chatter frequencies in milling processes, Int. J. Mach. Tool Manufact. 51 (2011) 457–464, https://doi.org/10.1016/j.ijmachtools.2011.02.002.
- [17] J. Feng, M. Wan, T.-Q. Gao, W.-H. Zhang, Mechanism of process damping in milling of thin-walled workpiece, Int. J. Mach. Tool Manufact. 134 (2018) 1–19, https://doi.org/10.1016/j.ijmachtools.2018.06.001
- [18] Y. Fu, Y. Zhang, H. Zhou, D. Li, H. Liu, H. Qiao, X. Wang, Timely online chatter detection in end milling process, Mech. Syst. Signal Process. 75 (2016) 668–688, https://doi.org/10.1016/j.ymssp.2016.01.003.
- [19] A. Honeycutt, T.L. Schmitz, Milling stability interrogation by subharmonic sampling, J. Manuf. Sci. Eng. 139 (2017), https://doi.org/10.1115/1.4034894.
- [20] T.L. Schmitz, M.A. Davies, K. Medicus, J. Snyder, Improving high-speed machining material removal rates by rapid dynamic analysis, CIRP Ann 50 (2001) 263–268, https://doi.org/10.1016/S0007-8506(07)62119-2.

- [21] N.E. Huang, Z. Shen, S.R. Long, M.C. Wu, H.H. Shih, Q. Zheng, N.-C. Yen, C. C. Tung, H.H. Liu, The empirical mode decomposition and the Hilbert spectrum for nonlinear and non-stationary time series analysis, Proc. R. Soc. London. Ser. A Math. Phys. Eng. Sci. 454 (1998) 903–995, https://doi.org/10.1098/spa.1998.0193.
- [22] P. Zhou, M. Du, S. Chen, Q. He, Z. Peng, W. Zhang, Study on intra-wave frequency modulation phenomenon in detection of rub-impact fault, Mech. Syst. Signal Process. 122 (2019) 342–363, https://doi.org/10.1016/j.ymssp.2018.12.011.
- [23] G. Tu, X. Dong, S. Chen, B. Zhao, L. Hu, Z. Peng, Iterative nonlinear chirp mode decomposition: a Hilbert-Huang transform-like method in capturing intra-wave modulations of nonlinear responses, J. Sound Vib. 485 (2020) 115571, https://doi. org/10.1016/j.jsv.2020.115571.
- [24] A.R. Messina, V. Vittal, Nonlinear, non-Stationary analysis of interarea oscillations via Hilbert spectral analysis, IEEE Trans. Power Syst. 21 (2006) 1234–1241, https://doi.org/10.1109/TPWRS.2006.876656.
- [25] A. Veltcheva, C. Guedes Soares, Nonlinearity of abnormal waves by the hilbert–huang transform method, Ocean Eng. 115 (2016) 30–38, https://doi.org/ 10.1016/j.oceaneng. 2016.01.031.
- [26] H.-T. Hsu, W.-K. Lee, K.-K. Shyu, T.-K. Yeh, C.-Y. Chang, P.-L. Lee, Analyses of EEG oscillatory activities during slow and fast repetitive movements using holo-Hilbert spectral analysis, IEEE Trans. Neural Syst. Rehabil. Eng. 26 (2018) 1659–1668, https://doi.org/10.1109/TNSRE.2018.2855804.
- [27] K. Dragomiretskiy, D. Zosso, Variational mode decomposition, IEEE Trans. Signal Process. 62 (2014) 531–544, https://doi.org/10.1109/TSP.2013.2288675.
- [28] I. Daubechies, J. Lu, H.T. Wu, Synchrosqueezed wavelet transforms: an empirical mode decomposition-like tool, Appl. Comput. Harmon. Anal. 30 (2011) 243–261, https://doi.org/10.1016/j.acha.2010.08.002.
- [29] N.E. Huang, Z. Shen, S.R. Long, A new view of nonlinear water waves: the Hilbert spectrum, Annu. Rev. Fluid Mech. 31 (1999) 417–457, https://doi.org/10.1146/ annurev.fluid.31.1.417.
- [30] F. Chu, W. Lu, Stiffening effect of the rotor during the rotor-to-stator rub in a rotating machine, J. Sound Vib. 308 (2007) 758–766, https://doi.org/10.1016/j. isv.2007.03.059.
- [31] M. Abramowitz, I.A. Stegun, Handbook of Mathematical Functions with Formulas, Graphs, and Mathematical Tables, US Government printing office, 1948.
- [32] B. Yan, L. Zhu, Research on milling stability of thin-walled parts based on improved multi-frequency solution, Int. J. Adv. Manuf. Technol. 102 (2019) 431–441, https://doi.org/10.1007/s00170-018-03254-0.
- [33] R.P.H. Faassen, N. van de Wouw, J.A.J. Oosterling, H. Nijmeijer, Prediction of regenerative chatter by modelling and analysis of high-speed milling, Int. J. Mach. Tool Manufact. 43 (2003) 1437–1446, https://doi.org/10.1016/S0890-6955(03) 00171 8

- [34] M.A. Davies, B. Balachandran, Impact dynamics in milling of thin-walled structures, Nonlinear Dynam. 22 (2000) 375–392, https://doi.org/10.1023/A: 1008364405411
- [35] J. Gradišek, M. Kalveram, T. Insperger, K. Weinert, G. Stépán, E. Govekar, I. Grabec, On stability prediction for milling, Int. J. Mach. Tool Manufact. 45 (2005) 769–781, https://doi.org/10.1016/j.ijmachtools.2004.11.015.
- [36] S. Chen, X. Dong, Z. Peng, W. Zhang, G. Meng, Nonlinear chirp mode decomposition: a variational method, IEEE Trans. Signal Process. 65 (2017) 6024–6037, https://doi.org/10.1109/TSP.2017.2731300.
- [37] R.T. Rockafellar, A dual approach to solving nonlinear programming problems by unconstrained optimization, Math. Program. 5 (1973) 354–373, https://doi.org/ 10.1007/RF01580138
- [38] V.E. Zakharov, A.I. Dyachenko, A.O. Prokofiev, Freak waves as nonlinear stage of Stokes wave modulation instability, Eur. J. Mech. B Fluid 25 (2006) 677–692, https://doi.org/10.1016/j.euromechflu.2006.03.004.
- [39] A. Hu, L. Xiang, Y. Zhang, Experimental study on the intrawave frequency modulation characteristic of rotor rub and crack fault, Mech. Syst. Signal Process. 118 (2019) 209–225, https://doi.org/10.1016/j.ymssp.2018.08.051.
- [40] S. Loutridis, E. Douka, L.J. Hadjileontiadis, Forced vibration behaviour and crack detection of cracked beams using instantaneous frequency, NDT E Int. 38 (2005) 411–419, https://doi.org/10.1016/j.ndteint.2004.11.004.
- [41] A.H. Nayfeh, D.T. Mook, Nonlinear Oscillations, John Wiley & Sons, 2008.
- [42] A. Honeycutt, T.L. Schmitz, Milling bifurcations: a review of literature and experiment, J. Manuf. Sci. Eng. 140 (2018), https://doi.org/10.1115/1.4041325.
- [43] Z.Z. Chen, Z.L. Li, J.B. Niu, L.M. Zhu, Chatter detection in milling processes using frequency-domain Rényi entropy, Int. J. Adv. Manuf. Technol. 106 (2020) 877–890, https://doi.org/10.1007/s00170-019-04639-5.
- [44] H. Cao, Y. Lei, Z. He, Chatter identification in end milling process using wavelet packets and Hilbert-Huang transform, Int. J. Mach. Tool Manufact. 69 (2013) 11–19, https://doi.org/10.1016/j.ijmachtools.2013.02.007.
- [45] T.Y. Hou, Z. Shi, P. Tavallali, Sparse time frequency representations and dynamical systems, Commun. Math. Sci. 13 (2015) 673–694, https://doi.org/10.4310/ CMS.2015.v13.n3.a4.
- [46] S.L. Brunton, J.L. Proctor, J.N. Kutz, Discovering governing equations from data by sparse identification of nonlinear dynamical systems, Proc. Natl. Acad. Sci. Unit. States Am. 113 (2016) 3932–3937, https://doi.org/10.1073/pnas.1517384113.
- [47] T.L. Schmitz, J. Couey, E. Marsh, N. Mauntler, D. Hughes, Runout effects in milling: surface finish, surface location error, and stability, Int. J. Mach. Tool Manufact. 47 (2007) 841–851, https://doi.org/10.1016/j.ijmachtools.2006.06.014.
- [48] Y. Altintas, E. Budak, Analytical prediction of stability lobes in milling, CIRP Ann 44 (1995) 357–362, https://doi.org/10.1016/S0007-8506(07)62342-7.